



One-pot, cascade conversion of cellulose to γ -valerolactone over a multifunctional Ru–Cu/zeolite-Y catalyst in supercritical methanol

Neha Karanwal^a, Rizky Gilang Kurniawan^c, Jaeyong Park^b, Deepak Verma^{b,c}, Suryun Oh^d, Seung Min Kim^d, Sang Kyu Kwak^e, Jaehoon Kim^{a,b,c,*}

^a SKKU Advanced Institute of Nanotechnology (SAINT), Sungkyunkwan University, 2066 Seobu-Ro, Jangan-Gu, Suwon, Gyeong Gi-Do 16419, Republic of Korea

^b School of Mechanical Engineering, Sungkyunkwan University, 2066 Seobu-Ro, Jangan-Gu, Suwon, Gyeong Gi-Do 16419, Republic of Korea

^c School of Chemical Engineering, Sungkyunkwan University, 2066, Seobu-Ro, Jangan-Gu, Suwon, Gyeong Gi-Do 16419, Republic of Korea

^d Institute of Advanced Composite Materials, Korea Institute of Science and Technology, Chudong-ro 92, Bongdong-eup, Wanju-gun, Jeonranbuk-do, Republic of Korea

^e School of Energy and Chemical Engineering, Ulsan National Institute of Science and Technology, Ulsan 44919, Republic of Korea

ARTICLE INFO

Keywords:

Cellulose
 γ -Valerolactone
Bimetallic Ru–Cu catalyst
Zeolite Y
One-pot conversion

ABSTRACT

A one-pot cascade conversion of cellulose to GVL was investigated over bimetallic Ru–Cu deposited on a zeolite Y (Ru–Cu/Z) catalyst. Under supercritical methanol conditions, high-yield (49.8%) cascade conversion of cellulose to GVL was achieved at 250 °C, with an initial H₂ pressure of 3.0 MPa and reaction time of 5 h. The Ru–Cu/Z catalyst was synthesized using activated reductive deposition (ARD), which resulted in the selective deposition of Cu nanodomains on Ru nanoparticles, thereby facilitating the dissociative adsorption of H₂. In addition, Lewis and Brønsted acid sites of Cu-doped zeolite Y effectively proceeded to cascade conversion reactions, including alcoholysis, isomerization, dehydration, and acetalization reactions, suppressing humin formation. The bimetallic Ru–Cu/Z catalyst was used in six consecutive runs, with a marginal loss of activity. The structure–performance relationships of the Ru–Cu/Z catalysts synthesized using ARD, incipient wet impregnation, and reduction deposition methods were compared.

1. Introduction

The catalytic conversion of lignocellulosic biomass to renewable chemicals and fuels is one of the most promising approaches for addressing the current global warming issues caused by the excessive use of fossil resources [1]. Cellulose, which is the major constituent of lignocellulosic biomass, consists of high-molecular-weight linear chains of glucose units connected by 1,4- β glycosidic linkage. However, it is challenging to directly convert cellulose into fuels and value-added chemicals with high selectivity due to its highly robust three-dimensional network of intermolecular hydrogen bonds, polymeric structure, and insolubility in most solvents [2–5]. Therefore, several consecutive reactions are required to achieve highly selective conversion of cellulose to targeted products. Furthermore, various undesirable side reactions can occur during cellulose conversion if the reaction pathways are not well controlled. γ -Valerolactone (GVL), a valuable target chemical obtained from cellulose, has attracted significant attention as a food additive, renewable solvent, and intermediate to

produce fragrance, drugs, fine chemicals, liquid transportation fuels, and building blocks for polymers [6–10]. However, as shown in Fig. 1, to achieve cellulose to GVL conversion, the following consecutive reactions are required to proceed over a multifunctional catalyst in methanol: (1) alcoholysis of cellulose to methyl D-glucopyranoside (MDG) over Brønsted acid sites (BASs) and Lewis acid sites (LASs); (2) isomerization of MDG to methyl D-fructofuranoside (MDFF) over LASs; (3) dehydration of MDFF to 5-methoxy methyl furfural (5-MMF) over BASs; (4) alcoholysis of 5-MMF to methyl levulinate (MLU) over LASs and BASs; and (5) dealcoholization and subsequent hydrogenation of MLU to GVL over BASs and metal sites. The direct conversion of cellulose to GVL can result in various other side products, such as 5-methyl furfural (5-MF), 5-methylfurfuryl alcohol (5-MFA), 2,5-dimethyl furan (2,5-DMF), 2,5-hexanedione (2,5-HDO), furfural (FFA), furfural alcohol (FOL), and cyclopentanone (CPO) (Fig. S1). In addition, if the desired reaction is not sufficiently controlled, the ring-opening of GVL and subsequent hydrogenation can produce methyl valerate (MV).

Various strategies for controlling the reaction pathways during the

* Correspondence to: School of Mechanical Engineering, School of Chemical Engineering, and SKKU Advanced Institute of Nanotechnology (SAINT), Sungkyunkwan University, 2066 Seobu-Ro, Jangan-Gu, Suwon, Gyeong Gi-Do 16419, Republic of Korea.

E-mail address: jaehoonkim@skku.edu (J. Kim).

<https://doi.org/10.1016/j.apcatb.2022.121466>

Received 27 February 2022; Received in revised form 27 April 2022; Accepted 29 April 2022

Available online 4 May 2022

0926-3373/© 2022 Elsevier B.V. All rights reserved.

one-step conversion of levulinic acid (LA) or levulinic esters (LEs) to GVL have been investigated using homogeneous and heterogeneous catalysts [9]. Although high-yield GVL can be obtained from LA and LEs, the LA feedstock is typically produced from cellulose in an aqueous medium with the addition of mineral acids (e.g., H_2SO_4) [11]. The recovery of LA from an aqueous mineral acidic solution of high purity is required to suppress the potential detrimental effect on the catalytic conversion of LA to GVL. The direct conversion of FFA/FOL to GVL [12] and monosaccharides (e.g., glucose, fructose, xylose) to GVL [13] was later proposed over bifunctional catalysts that contain acidic and metal sites. Considering that cellulose is the major non-edible source of the reaction intermediates (e.g., LA/LEs, FFA/FOL, and monosaccharides) for producing GVL, one-pot, direct conversion of cellulose to GVL, which can avoid the high-cost, energy-intensive, and time-consuming separation and purification of the intermediates, is the most desirable approach. However, only a few studies have focused on the one-pot conversion of cellulose to GVL (Table S1) [2–5]. For example, conversion of cellulose to GVL over a mixed trifluoroacetic acid (TFA) and Ru/C catalyst at 180 °C in a mixture of formic acid and water at H_2 pressure of 6.0 MPa resulted in a GVL yield of 29% [2]. When a mixture of strong Brønsted acidic heteropolyacid ($\text{H}_3\text{PW}_{12}\text{O}_{40}$) and Ru/ TiO_2 was used, a GVL yield of 40.5% was achieved at 150 °C in a mixture of γ -butyrolactone and water at H_2 pressure of 4.0 MPa [3]. Using a mixture of $\text{Al}_2(\text{SO}_4)_3$ and Ru/ ZrO_2 and microwave heating at 800 W, a high GVL yield of 51.2% was achieved in a mixture of isopropanol and water at 180 °C, whereas with conventional thermal heating, the GVL yield was significantly lower (2.7%) [4]. When Ag-exchanged $\text{H}_3\text{PW}_{12}\text{O}_{40}$ and Co–Ni nanoparticles encapsulated in a N-doped graphene layer were used as the catalyst mixture, a high GVL yield (55.9%) was achieved at 200 °C and N_2 pressure of 1.0 MPa for 9 h in water [5]. As mentioned, most previous studies on direct cellulose-to-GVL conversion used mixed acidic homogeneous/heterogeneous and metallic heterogeneous catalyst systems, which make it cumbersome to recover and reuse the catalyst mixture. In addition, possible metal leaching by the incorporation of acidic homogeneous catalysts should be carefully addressed. Therefore, it is highly desirable to develop an efficient, robust, and single-type multifunctional heterogeneous catalyst for one-pot conversion of cellulose to GVL.

Herein, we demonstrate that bimetallic Ru–Cu on zeolite Y is a highly efficient and robust catalyst for one-pot conversion of cellulose to GVL under supercritical methanol conditions. Supercritical methanol offers a fast reaction rate and suppresses humin or coke formation, which can maintain the active catalyst surface, owing to its unique physicochemical properties, such as low viscosity, zero surface tension, hydrogen donation ability, and high reactivity (e.g., esterification, alkylation, alkoxylation, and deoxygenation) [14].

The rationale for designing bimetallic Ru–Cu on zeolite Y catalyst includes: (1) balanced LASSs and BASs of the zeolite can control cellulose and intermediate conversion; (2) removal of residual Cl^- ions that have a detrimental effect on the catalyst activity; and (3) control of metal sites for hydrogenation. By considering the catalyst design rationale, a high

GVL yield of 49.8% was achieved at 250 °C with an initial H_2 pressure of 3 MPa and reaction time of 5 h. To examine the relationship between the catalyst synthesis method and catalytic performance, bimetallic Ru–Cu on zeolite Y catalyst was synthesized using three different methods: wet impregnation (WI), reductive deposition (RD), and activated reductive deposition (ARD). In the following sections, the effects of the catalyst synthesis method on the properties and activity of the catalysts in cellulose conversion are discussed. In addition, various reaction conditions were explored to achieve high GVL yields. Reaction mechanisms are proposed based on the conversion of potential reaction intermediates. Density functional theory (DFT) calculations were performed to gain insight into H_2 dissociation on bimetallic catalysts with different geometries.

1.1. Materials and characterization methods

The Supplementary Data document contains detailed descriptions of the materials used, catalyst evaluation, product analysis, and catalyst characterization methods, including X-ray diffraction (XRD), N_2 adsorption–desorption, field-emission scanning electron microscopy (FE–SEM), high-resolution transmission electron microscopy (HR–TEM), high-angle annular dark-field scanning transmission electron microscopy (HAADF–STEM) coupled with energy-dispersive X-ray spectroscopy (EDS), X-ray photoelectron spectroscopy (XPS), X-ray absorption spectroscopy (XAS), inductively coupled plasma-optical emission spectroscopy (ICP–OES), temperature-programmed desorption of ammonia and hydrogen (NH_3 -TPD, H_2 -TPD), H_2 temperature-programmed reduction (H_2 -TPR), pyridine-adsorbed diffuse reflectance infrared Fourier transform (pyridine–DRIFT), CO–DRIFT, thermogravimetric analysis (TGA), gas chromatography time of flight-mass spectroscopy (GC/TOF–MS), and GC equipped with a flame ionization detector (GC–FID).

1.2. Synthesis of the catalyst

The monometallic Cu and bimetallic Cu–Ru catalysts were synthesized using the WI, RD, and ARD methods. The catalysts are denoted as $x\text{R–}y\text{C/Z}(z)$, where x and y are the metal loadings of Ru and Cu, respectively, and z is the Si/Al ratio of zeolite Y. In a typical synthesis of 2 wt% Cu on zeolite Y using the WI method, 73.0 mg of Cu (NO_3) $_2 \cdot 2.5\text{H}_2\text{O}$ was dissolved in 2 mL of distilled and deionized (DDI) water, and then 0.98 g of zeolite Y was added to the Cu salt solution. The pH of the solution was 5.2; this pH was appropriate to exchange the acid sites of zeolite with Cu^{2+} species [15]. The solution was stirred for 2 h at 25 ± 2 °C. Water was then slowly evaporated at 80 °C under stirring. The sample was further dried overnight in a vacuum oven at 80 °C, calcined at 450 °C at a ramp rate of 2 °C min^{-1} under an air flow of 30 mL min^{-1} , and then reduced under a 5% H_2/Ar flow at 30 mL min^{-1} for 4 h. The synthesized catalyst is denoted as 2 C/Z(z)-WI.

Bimetallic Ru–Cu on zeolite Y was synthesized using WI. In a typical

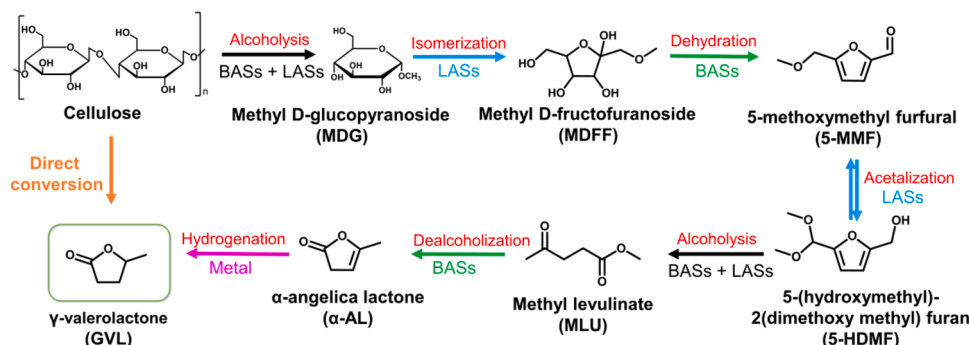


Fig. 1. Schematic pathway for the conversion of cellulose to GVL.

synthesis, 73.0 and 10.0 mg of $\text{Cu}(\text{NO}_3)_2 \cdot 2.5\text{H}_2\text{O}$ and $\text{RuCl}_3 \cdot x\text{H}_2\text{O}$, respectively, was dissolved in 2 mL of DDI water. After both salt mixtures were mixed, 0.975 g of zeolite Y was added to the mixed salt solution, and the solution was stirred for 2 h at $25 \pm 2^\circ\text{C}$. The pH of the solution mixture was 3.0; under low pH conditions, the zeolite surface was protonated ($^+\text{OH}_2$) [16]; thus, the strong electrostatic interaction between the protonated aluminosilicate framework and Cl^- ions makes it difficult for Cu and Ru ions to adsorb the aluminosilicate framework sites that were previously occupied with Cl^- ions [17]. After water was slowly evaporated at 80°C under stirring, the sample was further dried in a vacuum oven at 80°C overnight, calcined at 450°C for 4 h at a ramp rate of 2°C min^{-1} under an air flow of 30 mL min^{-1} , and then reduced under a 5% H_2/Ar flow at 30 mL min^{-1} for 4 h. The synthesized catalyst is denoted as 0.5R–2 C/Z(z)–WI.

Bimetallic Ru–Cu on zeolite Y catalysts was synthesized using the RD and ARD methods. To load 0.5 wt% Ru on calcined 2 C/Z(z), which was synthesized using the WI method, 10.0 mg of $\text{RuCl}_3 \cdot x\text{H}_2\text{O}$ was dissolved in 5 mL of DDI water and then 995.0 mg of the calcined 2 C/Z(z) sample was added to the aqueous Ru salt solution. Because of the acidic nature of Cl^- ions, the pH of the Ru salt solution was 1.8. The dispersion mixture was stirred for 15 min at $25 \pm 2^\circ\text{C}$. Then, 5 mL of an aqueous hydrazine hydrate solution at a concentration of 2 vol% was added dropwise to the Ru salt and 2 C/Z(z) dispersion mixture, and the entire solution was stirred for 6 h to proceed with hydrazine reduction. The pH of the solution increased from 1.8 to 9.2 during the addition of hydrazine hydrate. The addition of an aqueous hydrazine solution to the Ru salt dispersion mixture formed $[\text{Ru}(\text{NH}_3)_5\text{N}_2]^{2+}$ and $[\text{Ru}(\text{NH}_3)_6]^{2+}$ complexes [18,19]. Owing to the strong electrostatic attraction between the negatively charged 2 C/Z(z) surface (because of the loss of protons at high pH [20]) and the positively charged Ru cation complexes, controlled deposition of the Ru complex and subsequent nucleation and growth of ultrasmall metallic Ru nanoparticles (NPs) on the surface of 2 C/Z could occur [21,22]. In addition, the strong electrostatic repulsion between Cl^- ions and the negatively charged 2 C/Z surface suppressed

1.3. Catalytic reactions and product analysis

All catalytic reactions were performed in a 140-mL high-pressure autoclave equipped with a magnetic stirrer. In a typical experiment, 2 g cellulose, 0.5 g catalyst, and 30 mL methanol were added to the reactor. The reactor was purged with N_2 thrice to remove O_2 from the reactor head and then pressurized with H_2 at the desired pressure. The reactor was then heated to the desired temperature at a rate of $10^\circ\text{C min}^{-1}$. When the reactions were completed after the desired times, they were terminated by rapidly cooling the reactor in an ice-water bath. After the temperature reached $25 \pm 2^\circ\text{C}$, the gas in the reactor was evacuated. After opening the reactor, dodecane as an internal standard was added to the reaction mixture. The reaction mixture was collected in a beaker by washing the reactor with methanol. The catalyst was then separated from the reaction mixture using a centrifuge for 5 min, and the liquid product was analyzed using an Agilent 7890 N (Agilent, USA) gas chromatography (GC) instrument and a Pegasus (LECO, USA) high-throughput the time-of-flight mass spectroscopy (TOF-MS) system equipped with an auto injector system and Rxi-5Sil-MS column (Restek, USA, $30\text{ m} \times 0.25\text{ mm} \times 0.25\text{ }\mu\text{m}$). Typically, $2\text{ }\mu\text{L}$ of the liquid product was injected into the column in 25:1 split mode. The injector and transfer line temperatures were set to 250 and 260°C , respectively. The column temperature was programmed to start heating to 40°C , maintain the temperature for 2 min, and then increase the temperature to 300°C at a rate of $10^\circ\text{C min}^{-1}$. Reaction products were quantitatively determined using an Agilent 6890 N GC instrument (Agilent, USA) equipped with a Rxi-5Sil-MS capillary column (Restek, $30\text{ m} \times 0.25\text{ }\mu\text{m} \times 0.25\text{ mm}$) and a flame ionization detector (FID). The products were quantitatively determined by calibrating the column with corresponding standard chemicals. The cellulose conversion, product yield, and carbon balance of the products were calculated using the GC–FID results and the following equation:

$$\text{Conversion } (\%) = 1 - \left(\frac{\text{wt. of residue (g)} - \text{initial wt. of catalyst (g)}}{\text{initial wt. of feed (g)}} \right) \times 100, \quad (1)$$

undesirable chlorine deposition. The synthesized catalyst was then collected by filtering and washed with DDI water several times to remove Cl^- ions from the catalyst surface [23,24]. The catalyst was dried in a vacuum oven for 24 h at 80°C . The synthesized catalyst was denoted as 0.5R–2 C/Z(z)–RD. To completely reduce the metal NPs, the 0.5R–2 C/Z(z)–RD catalyst was calcined at 450°C with a ramp rate of 2°C min^{-1} in an air flow of 30 mL min^{-1} , and then reduced with a 5% H_2/Ar flow of 30 mL min^{-1} for 4 h. The thermally activated catalyst is denoted as 0.5R–2 C/Z(z)–ARD. The monometallic Ru on zeolite Y, designated as xRu/Z(z)–ARD, was synthesized using the same procedure used to synthesize 0.5R–2 C/Z(z)–ARD.

To investigate the role of zeolite Y in cellulose conversion, other types of supports were used, such as commercially available $\gamma\text{-Al}_2\text{O}_3$ and synthesized porous silica (PS) [25]. For the synthesis of PS, 0.5 g Pluronic P-123 was dissolved in 4 mL of DDI water, and 13.3 mL of an aqueous HCl solution was added to the solution under stirring. After stirring for 1 h, 1.15 mL of tetraethyl orthosilicate was added dropwise to the Pluronic P-123 and HCl solutions, and the entire solution was stirred for 24 h at approximately 35°C . The solid product was recovered by centrifugation, washed with DDI water, and dried at 80°C for 24 h. The dried product was calcined at 550°C for 5 h at a flow rate of 30 mL min^{-1} . The catalysts synthesized using the $\gamma\text{-Al}_2\text{O}_3$ and PS supports are denoted as 0.5R–2C/ $\gamma\text{-Al}_2\text{O}_3$ –ARD and 0.5R–2C/PS–ARD, respectively.

$$\text{Product yields } (\%) = \left(\frac{\text{moles of product produced}}{\text{moles of initial feed}} \right) \times 100, \quad (2)$$

$$\text{Carbon balance } (\%) = \left(\frac{\text{moles of carbon of product detected}}{\text{moles of carbon of initial feed used}} \right) \times 100. \quad (3)$$

2. Results and discussions

2.1. Catalyst characterization

In the XRD patterns of the metal-loaded catalysts, the peaks at 6.3° , 10.3° , 12.1° , 15.9° , 19.0° , 21.7° , 24.1° , 27.5° , and 31.9° , which are associated with the framework of zeolite Y, did not change significantly compared to those of pristine zeolite Y (Fig. 2a), indicating that the zeolitic structure was maintained during the metal loading, calcination, and reduction. In the calcined 2C/Z(40)–WI catalyst, diffraction peaks associated with Cu oxide species were not observed, which indicates that the majority of Cu was present in ionic forms (e.g., Cu^{2+} and $[\text{Cu}(\text{OH})]^{+}$) that were coordinated with zeolitic lattice oxygen [26] or as CuO_x in an amorphous form. In addition, a small amount of Cu oxide (CuO_x) nanocrystallites (below the detection limit of the XRD instrument,

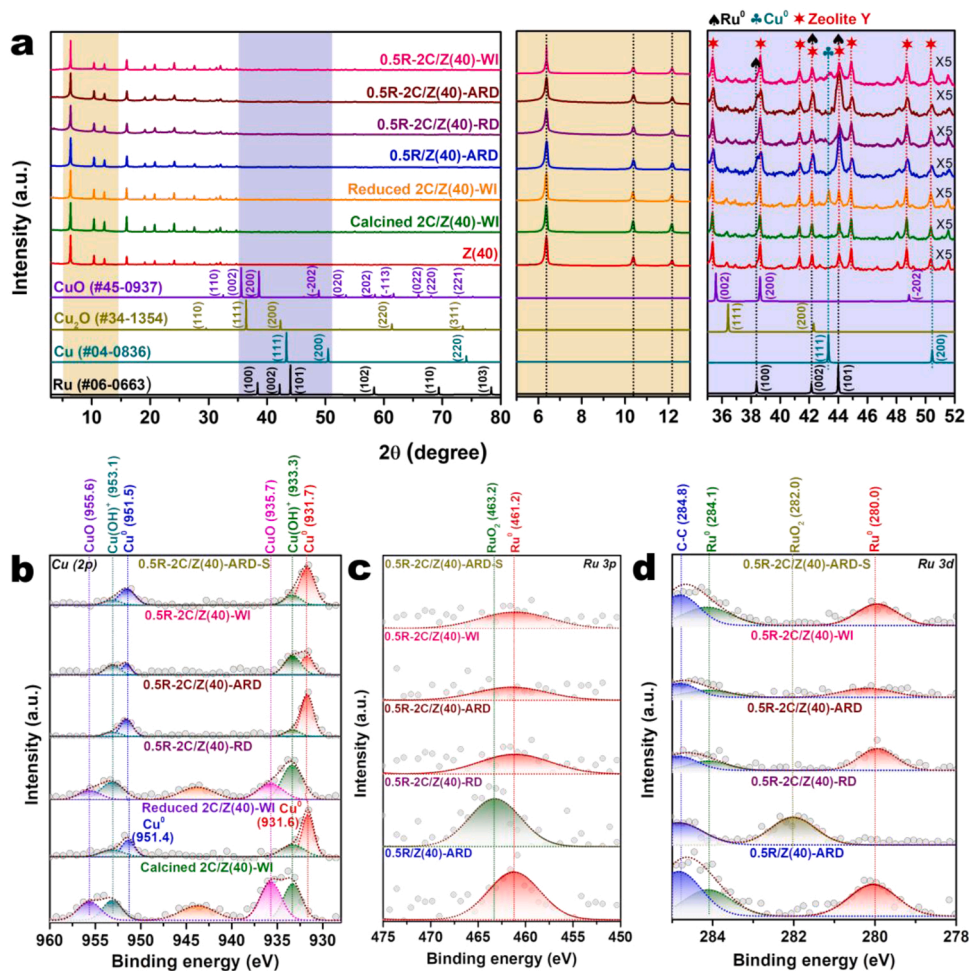


Fig. 2. (a) XRD patterns; (b) Cu 2p, (c) Ru 3p, and (d) Ru 3d high-resolution XPS core-level profiles of the mono- and bimetallic catalysts.

Table 1

Properties of the support and catalysts.

Catalyst	Ru/Cu crystallite size ^a (nm)	Ru/Cu particle size ^b (nm)	Textural properties					
			S _{BET} ^c (m ² g ⁻¹)	External surface area ^d	V _{total} ^e (cm ³ g ⁻¹)	d _{avg} ^f (nm)	Mesopore volume ^d (cm ³ g ⁻¹)	Micropore volume ^d (cm ³ g ⁻¹)
Zeolite Y	N.A./N.A. ^g	N.A./N.A.	770	112	0.5383	2.79	0.23	0.33
Calcined 2 C/Z (40)	N.A./N.A.	N.A./ 2–5	705	95	0.5300	3.00	0.21	0.32
Reduced 2 C/Z (40)	N.A./2.8	N.A./N.A.	702	95	0.5291	2.99	0.21	0.32
0.5 R/Z(40)–ARD	25.2/N.A.	25/N.A.	727	91	0.5237	2.87	0.19	0.33
0.5R–2 C/Z(40)–RD	N.A./N.A.	N.A./1–2	590	94	0.4624	3.17	0.20	0.27
0.5R–2 C/Z(40)–ARD	19.7/N.A.	22/0.2–1.0	619	90	0.5053	3.38	0.22	0.29
0.5R–2 C/Z(40)–WI	2.3/2.9	2.5/2.5	695	92	0.5348	3.07	0.21	0.32
0.5R–2 C/Z(40)–ARD–S ^h	20.7/N.A	22/0.2–1.0	509	75	0.3832	3.74	0.16	0.22

^a Measured using Cu (111) and Ru (100) planes and the Scherrer equation.

^b Measured using HR–TEM analysis.

^c S_{BET} = Brunauer–Emmet–Teller (BET) specific surface area.

^d Determined by the t-plot method.

^e V_{total} = total pore volume determined by the Barrett–Joyner–Halenda (BJH) method.

^f d_{avg} = average pore diameter determined by the BJH method.

^g N.A. = not applicable.

^h Spent catalyst collected after the 1st run without activation. Reaction conditions: 2 g cellulose, 0.5 g catalyst, 30 mL methanol, 250 °C, initial H₂ pressure of 3 MPa, 5 h.

~1 wt%) were dispersed in the zeolitic framework. The reduced 2C/Z(40)-WI catalyst showed an intense peak at 43.3° , which was associated with the (111) plane of Cu^0 (JCPDS file No. 04-0836). For the 0.5R/Z(40)-ARD catalyst, a peak at 38.4° was observed, and the peak at 44.0° became intense, which correspond to the (100) and (101) planes of Ru^0 (JCPDS file No. 06-0663), respectively. The 0.5R-2 C/Z(40)-RD catalyst did not show peaks associated with Cu^0 and Ru^0 due to the incomplete reduction of Cu oxides and $[\text{Ru}(\text{NH}_3)_5\text{N}_2]^{2+}$ to metallic Cu and Ru phases, respectively, or to the formation of ultrasmall Cu and Ru NPs that are below the detection limit of XRD. In the 0.5R-2C/Z(40)-ARD catalyst, the (100) and (101) planes of Ru^0 were observed, whereas those associated with Cu^0 or Cu oxides were not observed. When considering the high Cu loading of 0.5R-2C/Z(40)-ARD (1.9 wt%) and sufficient thermal reduction under the H_2/Ar flow condition, the absence of the peaks that are associated with Cu^0 indicates that ultrasmall Cu^0 nanodomains were synthesized using the ARD method. The 0.5R-2C/Z(40)-WI catalyst showed broad peaks at 43.3° and 38.4° , indicating that highly dispersed Cu^0 and Ru^0 NPs, respectively, were deposited on the zeolitic surface. The crystal sizes of Cu^0 and Ru^0 were calculated based on the (111) and (100) planes, respectively (Fig. S2), using the Scherrer equation; the results are listed in Table 1. The crystallite sizes of Ru in the 0.5 R/Z(40)-ARD and 0.5R-2C/Z(40)-ARD catalysts were much larger than those of Cu in the 2C/Z(40) and

0.5R-2C/Z(40)-ARD catalysts, implying that the weak interaction of the $[\text{Ru}(\text{NH}_3)_5\text{N}_2]^{2+}$ and $[\text{Ru}(\text{NH}_3)_6]^{2+}$ complexes with the support caused preferential interparticle aggregation of Ru. The presence of Cu suppresses the crystal growth of Ru to some extent.

The electronic states of the Cu and Ru species on the zeolite Y support were examined by XPS (Fig. 2b–d). XPS profiles were referenced to the main C 1s peak at 284.8 eV. The high-resolution Cu 2p XPS spectra of the calcined 2 C/Z(40)-WI catalyst had peaks associated with $\text{Cu}^{(2+)}\text{O}$ at 935.7 and 955.6 eV for Cu $2p_{3/2}$ and $2p_{1/2}$, respectively, and a $2p \rightarrow 3d$ shakeup satellite peak at 943.7 eV (Fig. 2b). The peak at the lower binding energies of 933.3 and 953.1 eV were attributed to the presence of $\text{Cu}(\text{OH})^+$ species, which can be incorporated in the Si–O–Al centers of zeolite Y by ion exchange [27]. The spectrum of the reduced 2 C/Z(40)-WI catalyst had peaks associated with Cu^0 at 931.6 and 951.4 eV for Cu $2p_{3/2}$ and $2p_{1/2}$, respectively [28], and peaks associated with $\text{Cu}(\text{OH})^+$. The absence of Cu^0 in the spectrum of the 0.5R-2 C/Z(40)-RD catalyst indicated that hydrazine reduction was not sufficient to form metallic Cu^0 . The Cu^0 $2p_{3/2}$ and $2p_{1/2}$ peaks in the 0.5R-2 C/Z(40)-ARD and 0.5R-2 C/Z(40)-WI catalyst upshifted to 931.7 and 951.5 eV, respectively, compared to those of reduced 2 C/Z(40)-WI (931.6 and 951.4 eV, respectively, Fig. S3). This was attributed to electron transfer from Cu to Ru and Cu to Cl owing to the higher electronegativity of Cl (3.16) and Ru (2.2) than that of Cu (1.9). The Ru 3p and Ru 3d spectra of

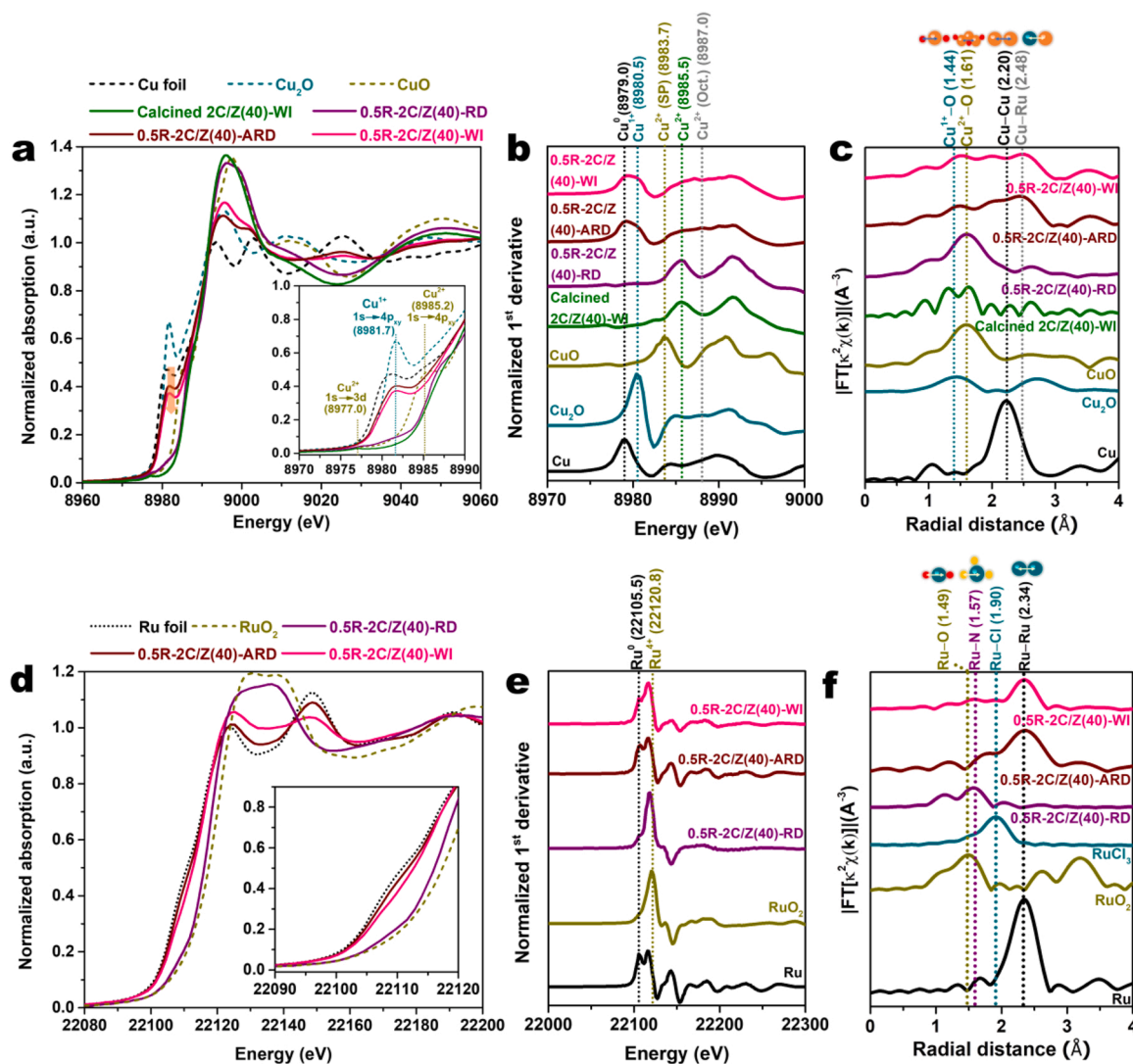


Fig. 3. (a) and (d) XANES profiles of Cu K-edge and Ru K-edge, respectively; (b) and (e) first-derivative XANES profiles of Cu K-edge and Ru K-edge, respectively; and (c) and (f) EXAFS profiles of Cu K-edge and Ru K-edge, respectively.

the 0.5 R/Z(40)–ARD catalyst included the peak associated with Ru⁰ at 461.2 and 280.0 eV, respectively (Fig. 2c and d) [29]. The peak at 463.2 eV in the 0.5R–2C/Z(40)–RD spectrum corresponds to Ru²⁺, which was attributed to the presence of [Ru(NH₃)₅N₂]²⁺ and [Ru(NH₃)₆]²⁺ complexes [18,19]. As shown in Fig. S4, the peak at 198.2 eV that corresponds to Cl 3p_{3/2} [30] was observed for the 0.5R–2 C/Z(40)–WI catalyst, while the Cl peak was not observed for the other catalysts. Thus, the catalyst synthesized using WI had residual Cl[−] ions on its surface. The amount of residual Cl[−] ions in the 0.5R–2 C/Z(40)–WI catalyst was 1.2 at% (Table S2).

The local chemical structures of Cu and Ru in the catalysts were analyzed by XAS, and the results are shown in Fig. 3. The Cu K-edge X-ray absorption near edge structure (XANES) spectrum of the calcined 2 C/Z(40)–WI sample had a weak pre-edge peak at 8977.0 eV and a relatively strong peak at 8985.2 eV, which are attributed to the Cu⁽²⁺⁾O species caused by dipole-forbidden 1 s → 3d and dipole-allowed 1 s → 4p_{xy} electron transitions, respectively [31,32]. The spectrum of 0.5R–2C/Z(40)–RD was similar to that of Cu⁽²⁺⁾O, indicating that the reducing power of hydrazine was not sufficiently high to form Cu⁰. The intensity of the pre-edge peaks of 0.5R–2C/Z(40)–ARD and 0.5R–2C/Z(40)–WI near 8981 eV was lower than that of the Cu foil, which could be due to the lower unoccupied density of the 4p states at their Fermi level owing to the coordination of Ru with Cu [33].

To clarify the chemical state of Cu in the catalysts, the 1st derivative of the Cu K-edge XANES spectrum is shown in Fig. 3b. The peaks at 8979.0, 8980.5, and 8983.7 eV correspond to the edge energies of the Cu⁰, Cu¹⁺, and Cu²⁺ species, respectively, in the square planar symmetry, and the peak at 8987.0 eV was assigned to the Cu²⁺ species in the octahedral symmetry [34]. The first-derivative spectra of the calcined 2 C/Z(40)–WI and 0.5R–2 C/Z(40)–RD catalysts did not have peaks associated with Cu²⁺ species in the square planar and octahedral symmetries, although a peak at 8985.5 eV was observed. This implies that the Cu²⁺ species in the catalysts are predominantly present in the distorted octahedral symmetry [34]. The 0.5R–2 C/Z(40)–ARD and 0.5R–2 C/Z(40)–WI catalysts contained Cu⁰ and Cu¹⁺ species, respectively. The Fourier-transformed *k*²-weighted spectra of the 0.5R–2 C/Z(40)–ARD and 0.5–2 C/Z(40)–WI catalysts and their corresponding references revealed the presence of a peak at 2.20 Å, attributed to the Cu–Cu scattering path, confirming the presence of Cu⁰. In addition, the presence of another strong Fourier-transformed peak at 2.48 Å in the spectra for the 0.5R–2 C/Z(40)–ARD and 0.5–2 C/Z(40)–WI catalysts implies the presence of a Cu–Ru scattering path, indicating some coordination between Cu and Ru atoms [35]. This peak was not observed in the spectra of calcined 2 C/Z(40)–WI and 0.5R–2 C/Z(40)–RD. The wavelet transforms of the *k*²-weighted profiles of the catalysts and their corresponding references were collected to examine the coordination environment of Cu in the catalysts (Fig. S5). The spectra of the 0.5–2 C/Z(40)–RD and 0.5–2 C/Z(40)–WI catalysts showed evidence of a much stronger Cu–O first-shell signal centered at 3.7 Å^{−1} and 1.5 Å, respectively, than that of the 0.5R–2 C/Z(40)–ARD catalyst, indicating that the Cu species in 0.5R–2 C/Z(40)–ARD was in a highly reduced state.

The pre-edge region of the Ru K-edge XANES spectra of 0.5–2 C/Z(40)–WI and 0.5R–2 C/Z(40)–ARD approached that of the Ru foil, indicating the presence of Ru⁰ (Fig. 3d). In contrast, the pre-edge region of the spectrum of 0.5R–2 C/Z(40)–RD approached that of RuO₂, indicating that the major Ru species was high-valent Ruⁿ⁺. A similar result was observed for the 1st derivative of the Ru K-edge XANES spectra (Fig. 3e). In the Fourier-transformed *k*²-weighted spectra, the intensity of the Ru–Ru scattering path at 2.34 Å of 0.5R–2 C/Z(40)–ARD was higher than that of 0.5R–2 C/Z(40)–WI, indicating a higher degree of Ru–Ru coordination in the ARD catalyst. In the 0.5R–2 C/Z(40)–RD spectrum, the peak at 1.57 Å, which was slightly larger than that of Ru–O (1.49 Å), was attributed to the scattering path of Ru–N in the [Ru(NH₃)₅N₂]²⁺ and [Ru(NH₃)₆]²⁺ complexes.

To quantify the surface area of the catalysts, N₂ adsorption–desorption isotherms were collected, and the results are shown in

Fig. S6 and Table 1. Zeolite Y showed a type-II isotherm with an H4-type hysteresis loop in the P/P₀ range of 0.45–1.0, indicating the presence of mesopores. The BET surface area of zeolite Y was 770 m² g^{−1}, and the external surface area was 112 m² g^{−1}, which corresponds to 15% of the total BET surface area. The 2 wt% Cu loading on zeolite Y reduced the BET surface area to 705 m² g^{−1}. The 0.5 wt% Ru loading did not significantly change the surface area of pristine zeolite Y. The 0.5R–2C/Z(40)–RD catalyst had a much lower BET surface area (590 m² g^{−1}) than those of 0.5R–2C/Z(40)–ARD (619 m² g^{−1}) and 0.5R–2C/Z(40)–WI (695 m² g^{−1}), because the uniformly dispersed ultrasmall Ru complex ([Ru(NH₃)₅N₂]²⁺) domains on the zeolitic framework blocked some micropores.

The overall morphologies of the catalysts were examined using FE–SEM and EDS. As shown in Fig. S7a and b, zeolite Y had a highly crystalline octahedral structure with particle sizes in the range of 0.4–0.6 μm. The overall morphology of zeolite Y was maintained after loading with Cu and Ru NPs (Fig. S7c–h). The presence of Cu and Ru was confirmed by EDS mapping (Fig. S7i). A highly ordered microporous framework of zeolite Y was observed from the HR–TEM image (Fig. S8). For the calcined 2 C/Z(40)–WI catalyst, spherical CuO_x NPs with sizes in the range of 2–5 nm were dispersed on the zeolite support (Fig. S9a and b). In addition, as shown in the HAADF–STEM image and corresponding EDS images (Fig. S9d–h), a uniform distribution of non-particulate Cu species on the surface of zeolite Y was observed, which suggests Cu ion exchange in the Si–(OH)–Al sites. The fast Fourier-transform (FFT) image shown in Fig. S9c indicates the amorphous nature of CuO_x, which agrees well with the XRD results. In the monometallic 0.5 R/Z(40)–ARD catalyst, interparticle agglomeration during the calcination and reduction of 0.5 R/Z(40)–RD caused the formation of large (~25 nm) irregular Ru NPs (Fig. S10).

For the bimetallic 0.5R–2C/Z(40)–RD catalyst, spherical CuO NPs (1–2 nm) were dispersed on the zeolite support (Fig. S11a–c). The barely observable Cl species indicated that residual Cl[−] was successfully removed by hydrazine treatment (Fig. S11d–h). In the 0.5R–2C/Z(40)–ARD catalyst, highly irregular metal particles were present on the external surface of zeolite Y (Fig. 4e). Hexagonal close-packed (hcp) Ru⁰ and face-centered cubic (fcc) Cu⁰ were identified from the FFT images (Fig. 4b and d). The interlayer spacing of 2.34 and 2.07 nm in Fig. 4c indicates the presence of the (100) plane of hcp Ru⁰ and (111) plane of fcc Cu⁰. The HAADF–STEM image and its corresponding EDS images indicated that Cu nanodomains with sizes of approximately 0.2–1.0 nm were deposited on the surface of the Ru NPs (Fig. 4e–i). During the air calcination and thermal H₂ reduction of 0.5R–2 C/Z(40)–RD, some of the Cu species present on the external surface or deposited within the micropores of zeolite Y migrated to the surface of the Ru NPs, forming a core–shell structure. It is not clear what causes this, but the much higher surface tension of Ru than Cu (Table S3) and the increased mobility of Cu at high temperatures [26,36] could be responsible for Cu migration to the surface of the Ru NPs. Considering the mutual immiscibility between Ru and Cu phases [37], the possibility of forming Ru–Cu alloys was excluded in this study. As shown in Fig. 4n, the 0.5R–2 C/Z(40)–WI catalyst had a different morphology than the 0.5R–2 C/Z(40)–ARD catalyst. Ultrasmall Cu and Ru NPs with an average size of 2.5 ± 0.2 nm were uniformly dispersed on the zeolitic support in the 0.5R–2 C/Z(40)–WI catalyst. Some of the Ru NPs were not covered by Cu domains (Fig. 4n–r).

Based on the discussion thus far, a schematic of the formation mechanism of Ru–Cu NPs on the zeolitic support is presented in Fig. 4s. The electronic state, morphology, and size of the Cu and Ru NPs depend on the chosen synthesis method. For the 0.5R–2 C/Z(40)–ARD catalyst, Cu was first deposited using the WI method. The low pH (5.2) during the impregnation of Cu ions favored Cu exchange to form Cu²⁺ and [Cu(OH)]⁺, which were coordinated with zeolitic lattice oxygen [26]. However, the possibility of forming amorphous CuO_x in the large-membered rings or on the external surface of zeolite Y should not be excluded. After Cu impregnation, Ru was deposited on the calcined

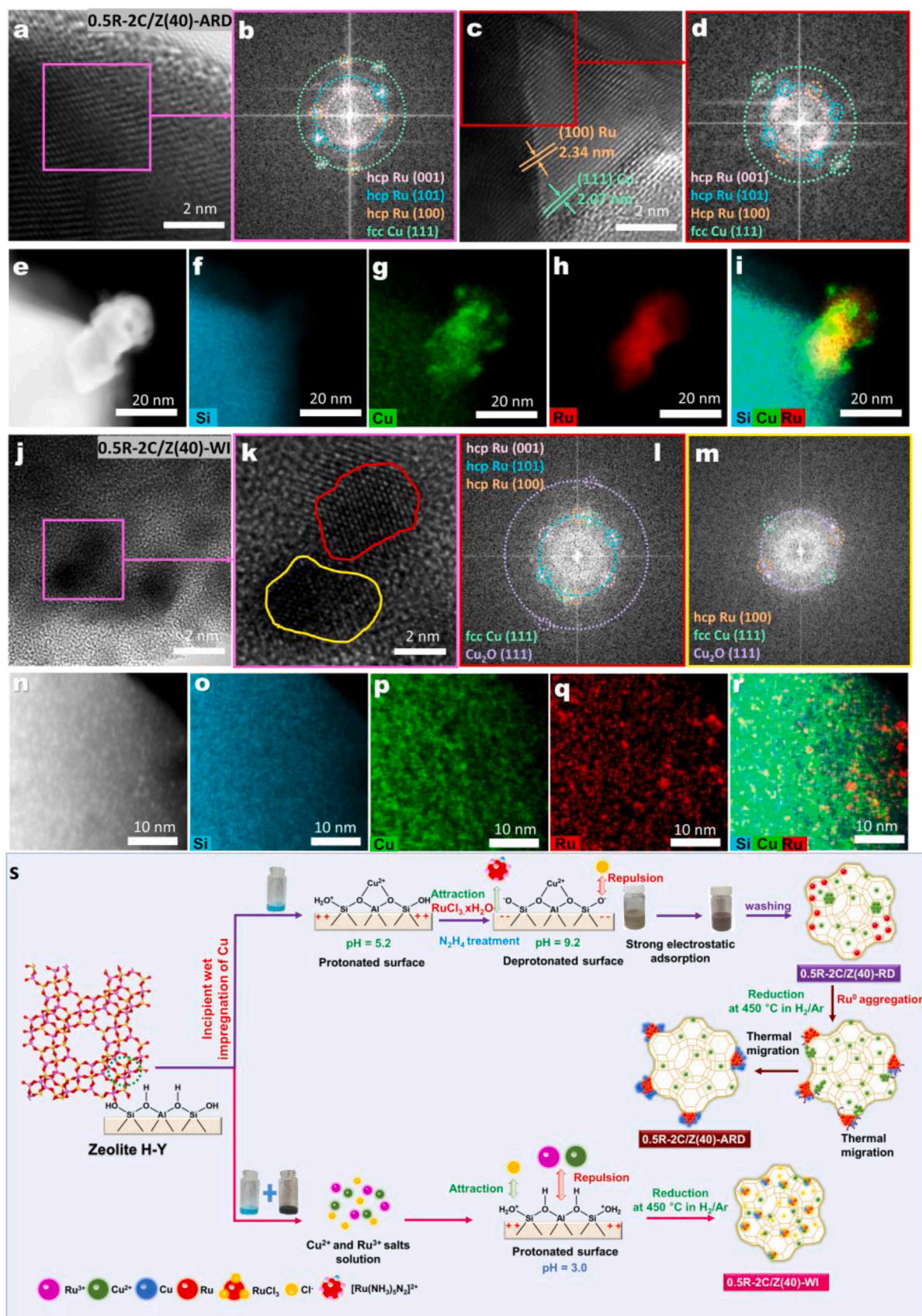


Fig. 4. (a–d) HR-TEM images and FFT patterns; and (e–i) HAADF-STEM and the corresponding EDS images of 0.5R-2C/Z(40)-ARD. (j–m) HR-TEM images and FFT patterns; and (n–r) HAADF-STEM and its corresponding EDS images of 0.5R-2C/Z(40)-WI. (s) Schematic of the synthesis process of 0.5R-2C/Z(40)-ARD and 0.5R-2C/Z(40)-WI catalysts.

2C/Z(40) catalyst using ARD. The reaction of Ru^{3+} with hydrazine forms $[\text{Ru}(\text{NH}_3)_5\text{N}_2]^{2+}$ and $[\text{Ru}(\text{NH}_3)_6]^{2+}$ complexes in the fluid phase [18, 19], which are adsorbed on the surface of 2C/Z(40). Because of the alkaline solution (pH 9.2) during hydrazine reduction, the zeolitic surface is deprotonated, resulting in electrostatic interactions between the Ru cation complexes and the negatively charged zeolitic surface [20]. During the thermal reduction of the Ru-cation-adsorbed 2C/Z(40), Ru NPs aggregated at the zeolitic surface, and Cu species migrated to the surface of the Ru NPs, forming Cu nanodomains. In the case of the 0.5R-2C/Z(40)-WI catalyst, Cu salt and Ru salt solutions were mixed, and then the mixed salts were impregnated into zeolite Y. Because of the low pH of the solution (3.0), the zeolite surface was protonated, and thus the favorable electrostatic interaction between Cl^- and the protonated surface made it difficult to remove residual Cl^- after calcination and reduction. Calcination of the impregnated Ru and Cu salts formed a bimetallic 0.5R-2C/Z(40)-WI catalyst with ultrasmall particles.

The properties of the acid sites in the catalyst were examined using NH_3 -TPD and pyridine-DRIFT analyses. During TPD analysis, the desorbed species were monitored using a quadrupole mass spectrometry (QMS) residual gas analyzer, and the profiles for NH_3 desorption were

corrected using the secondary mass profile of $m/z = 16$ (Fig. S12). Zeolite Y exhibited weak ($<250^\circ\text{C}$) and strong ($>250^\circ\text{C}$) acidic sites (Fig. 5a), which are attributed to the interaction of NH_3 with a cation-bonded silanol group (weak LAS) and a terminal silanol group (weak BAS), whereas the strong acidic sites are attributed to the interaction of NH_3 with acidic protons at the bridging $\text{Si}-(\text{OH})-\text{Al}$ sites (strong BAS) and extra Al framework of the $\text{Si}-(\text{O})-\text{Al}$ sites (strong LAS) [38,39]. The total acid strength of zeolite Y was $0.319 \text{ mmol g}^{-1}$ (Table 2). After loading 2 wt% Cu on zeolite Y, the number of weak acid sites increased, whereas the number of strong acid sites decreased compared to that of zeolite Y. The Cu ion exchange in the $\text{Si}-(\text{OH})-\text{Al}$ group suppressed the strong BAS, whereas the formation of $\text{Cu}(\text{OH})^+$ during the ion exchange increased the number of weak BASs. As compared to zeolite Y, the NH_3 desorption temperature of the 2Cu/Z(40)-WI catalyst downshifted, which imply that the NH_3 molecules were loosely bound with the Cu $(\text{OH})^+$ species and some CuO_x NPs presented on the surface of zeolite [40]. In the 0.5R/Z(40)-ARD catalyst, the number of both weak and strong acid sites decreased compared to those in zeolite Y, indicating that the acid sites were covered with Ru NPs. The preferential adsorption of $[\text{Ru}(\text{NH}_3)_5\text{N}_2]^{2+}$ and $[\text{Ru}(\text{NH}_3)_6]^{2+}$ complexes on the strong acid sites

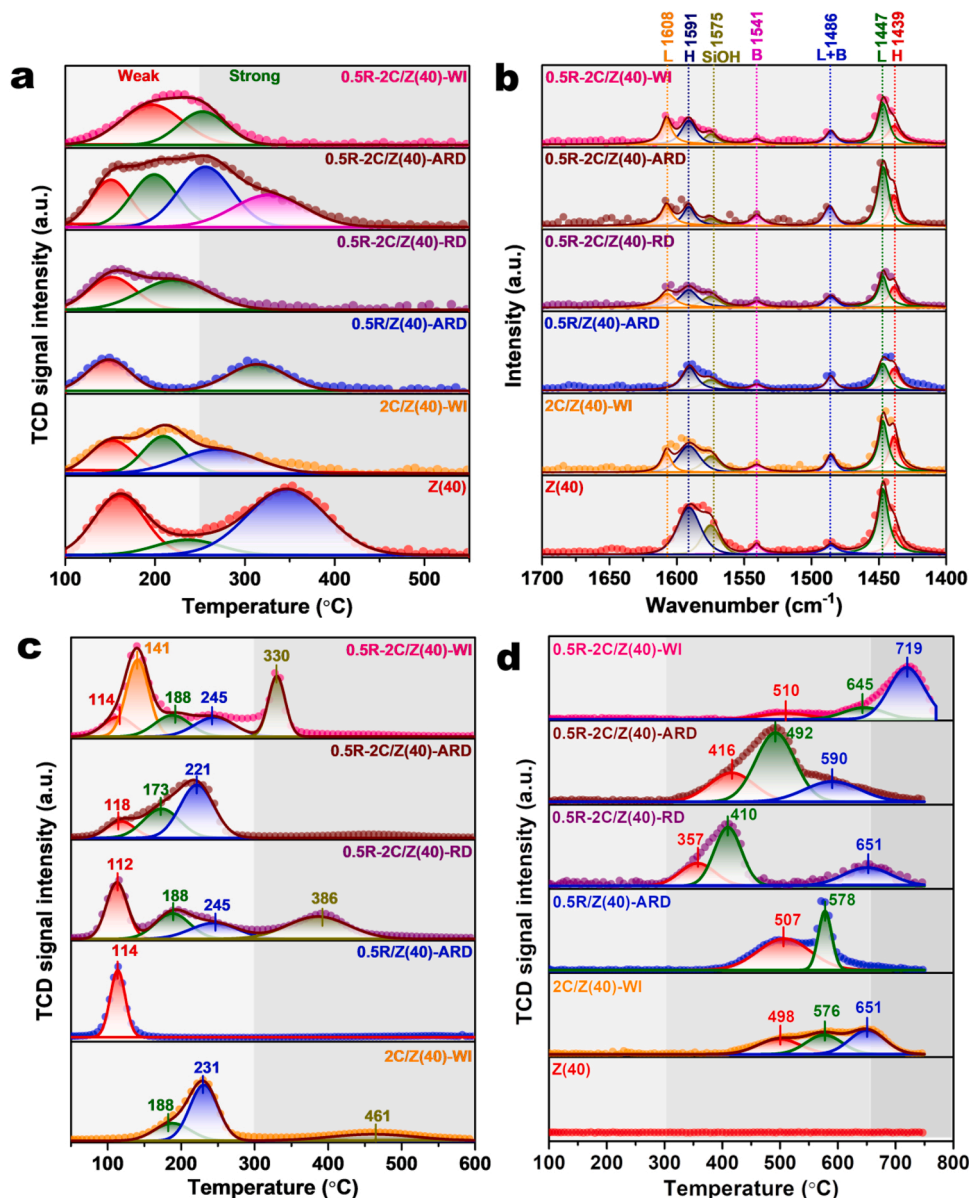


Fig. 5. (a) NH_3 -TPD, (b) pyridine-adsorbed DRIFT, (c) H_2 -TPR, and (d) H_2 -TPD profiles of the mono- and bimetallic catalysts.

Table 2Acidity, H₂ desorption, and H₂ reduction properties of the support and catalysts.

Catalyst	Acidity (mmol g ⁻¹) ^a			L/B ratio ^b	H ₂ desorption ^c (mmol g ⁻¹)	H ₂ uptake ^d (mmol g ⁻¹)	Metal loading (wt%) Ru/Cu ^e
	Weak	Strong	Total				
Zeolite Y	0.139	0.180	0.319	4.92	0.0	N.A.	N.A.
2 C/Z(40)-WI	0.146	0.057	0.203	5.18	0.211	3.33	0/2.2
0.5 R/Z(40)-ARD	0.074	0.095	0.170	3.06	0.161	0.82	0/2.2
0.5R-2 C/Z(40)-RD	0.138	0.036	0.173	5.42	0.227	5.33	0.6/0
0.5R-2 C/Z(40)-ARD	0.212	0.126	0.339	3.92	0.476	3.00	0.56/2.3
0.5R-2 C/Z(40)-WI	0.142	0.054	0.196	4.65	0.173	6.00	0.65/1.9
0.5R-2 C/Z(40)-ARD-S ^f	0.054	0.091	0.145	2.71	N.A. ^g	3.17	0.48/1.9
0.5R-2 C/Z(40)-ARD-A ^h	0.214	0.124	0.338	3.74	N.A.	N.A.	0.64/1.9

^a Measured by NH₃-TPD.^b L/B ratio = ratio of Lewis acid sites to Brønsted acid sites measured pyridine-DRIFT spectra.^c Hydrogen desorption was measured using H₂-TPD.^d Hydrogen consumption was measured using H₂-TPR.^e Measured using ICP-OES.^f Spent catalyst collected after the 1st run without activation. Reaction conditions: 2 g cellulose, 0.5 g catalyst, 30 mL methanol, 250 °C, initial H₂ pressure of 3 MPa, 5 h.^g N.A. = not available.^h Activated catalyst.

in the 0.5R-2C/Z(40)-RD catalyst reduced the strong acidity of zeolite Y. The 0.5R-2C/Z(40)-ARD catalyst exhibited a wide range of weak-to-strong acidity with a higher total acid strength (0.339 mmol g⁻¹) than that of zeolite Y. The increase in the amount of weak acidity can be caused by Cu nanodomains on the surface of the Ru NPs; because of the electron transfer from Cu to Ru, the weak Lewis acidic Cu^{δ+} species formed at the surface could adsorb the NH₃ molecules [41]. In addition, Cu migration could open up the strong acid sites of zeolite Y. In the case of 0.5R-2C/Z(40)-WI, the strong acid sites associated with zeolite Y were highly suppressed and the total acidity was much lower (0.196 mmol g⁻¹) than that of 0.5R-2C/Z(40)-ARD (0.339 mmol g⁻¹) because of the coverage of metal NPs on the zeolitic support and the undesirable adsorption of Cl⁻ ions.

In the pyridine-DRIFT spectra (Fig. 5b), the adsorption bands at 1439 and 1591 cm⁻¹ are associated with hydrogen-bonded LASs, the bands at 1447 and 1608 cm⁻¹ correspond to LASs, the band at 1541 cm⁻¹ was assigned to BASs, and the band at 1486 cm⁻¹ was ascribed to both LASs and BASs [42]. The band at 1575 cm⁻¹ corresponds to the pyridine interaction with the silanol group of zeolite [42]. The ratio of LASs to BASs (L/B) was estimated by integrating the areas of the adsorption bands at 1447 and 1541 cm⁻¹, respectively, and the results are listed in Table 2. The L/B ratio of the zeolite was high (4.92), indicating the dominance of LASs because of its high Si/Al ratio of 40. As the Si/Al ratio of zeolite Y decreased from 40 to 2.6 in the 0.5R-2 C/Z(z)-ARD catalysts, L/B decreased from 3.92 to 1.12 (Fig. S13). The intensity of the band at 1541 cm⁻¹ in the 2 C/Z(40)-WI catalyst was suppressed due to Cu ion exchange at the BASs, while the band at 1608 cm⁻¹ was observed, suggesting that pyridine molecules were coordinated to the Cu divalent cations [41,43]. The intensities of the bands associated with BASs and LASs in the 0.5 R/Z(40)-ARD and 0.5R-2 C/Z(40)-RD catalysts decreased owing to the coverage of the zeolite surface by Ru NPs and Ru complexes, respectively. The Cu migration to the surface of Ru NPs during the calcination of the 0.5R-2 C/Z(40)-RD catalyst could expose the BASs of zeolite Y, which resulted in a decrease in L/B from 5.42 (0.5R-2 C/Z(40)-RD) to 3.92 (0.5R-2 C/Z(40)-ARD). In contrast, L/B of the 0.5R-2 C/Z(40)-WI catalyst was higher (4.65) than that of 0.5R-2 C/Z(40)-ARD because residual Cl⁻ ions were deposited on the BASs.

The reduction properties of the oxidized catalysts were examined using H₂-TPR, and the results are presented in Fig. 5c and Table 2. The TPR spectrum of 2 C/Z(40)-WI had three peaks centered at 188, 231, and 461 °C. The peak at 188 °C is associated with the reduction of CuO to Cu⁺, which could be located in the super cages of zeolite Y; the peak at 231 °C was attributed to the reduction of ion-exchanged oxocations

[Cu²⁺-O-Cu²⁺], bulk CuO to Cu⁰, and/or CuO to Cu⁺ present in the sodalite cages of zeolite Y, while that at 461 °C was attributed to the reduction of Cu⁺ to Cu⁰ [44]. Based on the total amount of H₂ consumed and the Cu loading, 63.5% of the Cu was reduced to Cu⁰, whereas 36.5% of non-reducible Cu species were present in the zeolite framework via ion exchange. The spectrum of the 0.5R/Z(40)-ARD catalyst had an intense peak at 114 °C, which corresponds to the reduction of RuO₂ to Ru⁰. In the case of the spectra for 0.5R-2C/Z(40)-RD, 0.5R-2C/Z(40)-ARD, and 0.5R-2C/Z(40)-WI, the peaks at 112–114 °C were attributed to RuO₂ → Ru⁰, those at 173–188 °C were attributed to CuO → Cu⁺ located in the super cages, and those at 221–245 °C were attributed to ion-exchanged oxocations [Cu²⁺-O-Cu²⁺] and CuO → Cu⁺, which could be present in the sodalite cages. The spectra of the 0.5R-2C/Z(40)-RD and 0.5R-2C/Z(40)-WI catalysts had high-temperature peaks at 386 and 330 °C, respectively, which were attributed to Cu⁺ → Cu. The high-temperature Cu⁺ → Cu peak was not observed for the 0.5R-2C/Z(40)-ARD catalyst. In addition, the peaks associated with the reduction of Cu oxides were downshifted compared with those of the 2C/Z(40)-WI catalyst. The close proximity of the Cu and Ru domains in the core-shell structure enhanced the reducibility of Cu in 0.5R-2C/Z(40)-ARD. In case of 0.5R-2C/Z(40)-WI, an additional peak at 141 °C was observed; the origin of this is not clear, but it could be related to the reduction of Ru-Cl species [45,46]. The reduction temperatures of Ru and Cu species in 0.5R-2C/Z(40)-WI were higher than those in 0.5R-2C/Z(40)-ARD, which suggests that the residual Cl⁻ ions interfered with the reduction of metal species [46].

The H₂-TPD profiles of the catalysts are presented in Fig. 5d, and the amount of H₂ desorbed is listed in Table 2. The H₂-TPD profiles were divided into two regions: a low-temperature region at 100–300 °C, which is associated with physically adsorbed H₂, and a high-temperature region at >300 °C, which corresponds to chemisorbed H₂ and H₂ in the subsurface layers, and spillover H₂ [47]. The high-temperature peaks above 500 °C observed in the spectra of 2C/Z(40)-WI and 0.5R/Z(40)-ARD suggested that the majority of H₂ was present in the subsurface layer or H₂ spillover in the metallic sites [48,49]. The H₂ desorption peaks of the bimetallic 0.5R-2C/Z(40)-RD and 0.5R-2C/Z(40)-ARD catalysts were downshifted compared with those of the monometallic 2C/Z(40)-WI and 0.5 R/Z(40)-ARD catalysts. The low-temperature peaks at 357 and 410 °C in 0.5R-2C/Z(40)-RD were upshifted to 416 and 492 °C, respectively, in the 0.5R-2C/Z(40)-ARD catalyst, which could be due to larger metal NPs. In contrast, the high-temperature peak at 651 °C observed in the spectrum of 0.5R-2C/Z(40)-RD was downshifted to 590 °C for the 0.5R-2C/Z(40)-ARD catalyst, which could be due to the close proximity between the Cu and Ru

domains [35,36]. In addition, the total amount of H_2 desorbed from the 0.5R–2 C/Z(40)–ARD catalyst was approximately double ($0.476 \text{ mmol g}^{-1}$) that from 0.5R–2 C/Z(40)–RD ($0.227 \text{ mmol g}^{-1}$). The facilitated H_2 adsorption on the 0.5R–2 C/Z(40)–ARD catalyst is attributed to the close proximity between the Ru and Cu sites in the core-shell structure. The hydrogen molecules were first dissociated on Ru sites, and then the dissociated hydrogen atom spilled over to adjacent Cu sites; the weakly adsorbed H atoms on the Cu sites facilitate the desorption of H_2 at relatively lower temperatures. In the case of the 0.5R–2 C/Z(40)–WI catalyst, the weak broad peaks at 510 and 645 °C are associated with H_2 desorption, while the highly intense peak at high temperature (710 °C) was caused by the desorption of Cl^- ions as HCl (Fig. S14) [50]. Based on the peaks at 510 and 645 °C, the total amount of adsorbed H_2 was much lower ($0.173 \text{ mmol g}^{-1}$) than that of 0.5R–2C/Z(40)–ARD. The coverage of Cl^- on the surface of metal NPs and the electron-withdrawing nature of these ions could suppress H_2 adsorption on metallic sites [24,45,50].

DFT simulations were performed to gain insight into the favorable H_2 adsorption on the Cu nanodomains deposited on Ru NPs in the 0.5R–2 C/Z(40)–ARD catalyst. The structures of slabs of Cu(111), Ru(001), Cu islands on Ru(001) (denoted as Cu_1Ru), one layer of Cu on three-layer Ru(001) (denoted as Cu_1Ru_3), and two-layer Cu on two-layer Ru(001) (denoted as Cu_2Ru_2) are shown in Fig. S15. H_2 was weakly adsorbed in linear geometries on Cu(111), Ru(001), Cu_1Ru , Cu_1Ru_3 , and Cu_2Ru_2 , with adsorption energies of -0.0158 , -0.012 , -0.015 , -0.0152 and -0.0154 eV, respectively. The shortest distances between the Cu(111), Ru(001), Cu_1Ru , Cu_1Ru_3 , and Cu_2Ru_2 surfaces and H atom were 2.64, 2.86, 2.76, 2.50 and 2.65 Å, respectively (Fig. S16). The weak adsorption energy of molecular H_2 indicates that H_2 is preferentially dissociated into two H atoms that are adsorbed on the catalyst surface [51]. The DFT results for the adsorption of H atoms onto Cu(111), Ru(001), Cu_1Ru , Cu_1Ru_3 , and Cu_2Ru_2 are shown in Fig. S17. The H atom strongly adsorbed on the Cu(111), Ru(001), and Cu_1Ru surfaces with adsorption energies of -3.61 , -3.54 , and -3.69 , respectively, for the interface between Cu and Ru, and -3.62 eV for the Cu site next to the interface between Cu and Ru. Compared to the adsorption on the Cu(111), Ru(001), and Cu_1Ru surface, the H atom is weakly adsorbed on the Cu_1Ru_3 and Cu_2Ru_2 surfaces with adsorption energies of -3.29 and -3.32 eV, respectively. Electron transfer from Cu to Ru can cause weak adsorption of H atoms on the Cu layer. On the Cu(111) surface, the H atoms connected to three neighboring Cu atoms in the hollow hexagonal-close-packed Cu (HCP_{Cu}) site with a bond length of 0.90 Å, while on the Ru(001) surface, each H atom stayed in the hollow site without forming bonds with Ru atoms with a length of 1.05 Å. At the interface between the Cu and Ru domains of the Cu_1Ru surface, H atoms are adsorbed on the 3Ru and 1Cu hollow sites without forming bonds.

The energy values and reaction diagrams for dissociative H_2 adsorption on Cu(111), Ru(001), Cu_1Ru , Cu_1Ru_3 , and Cu_2Ru_2 are shown in Fig. S18. On the Cu(111) surface, H_2 dissociation occurs after exceeding the high activation barrier of 0.52 eV. After dissociation, two H atoms spilled over the neighboring hollow HCP_{Cu} sites with a final state energy of -0.45 eV. On the Ru(001) surface, H_2 dissociation occurred with a small activation barrier (0.03 eV) with a final state energy of -0.73 eV, suggesting that dissociative H_2 adsorption was highly favorable. The dissociative adsorption of H_2 on Cu_1Ru_3 and Cu_2Ru_2 slabs occurred with activation barriers of 0.49 and 0.51 eV, respectively, with a final state energy of -0.41 and -0.46 eV, respectively. As for the Ru(001) surface, H_2 dissociation was highly favorable with a small activation barrier of 0.05 eV and an energy state of -0.72 eV on the Ru site of the Cu_1Ru surface. The adsorbed H atom was then transferred to the interfacial site with a small activation barrier (0.28 eV) and a final state energy of -0.83 eV. The partial density of states (Fig. S19) shows that the d-band center of the Ru–Cu interface was closer to the Fermi level than the other adsorption cases; thus, strong H-atom adsorption on the Ru–Cu interfacial site can be expected because of the lower availability of electrons to fill the antibonding orbital of the

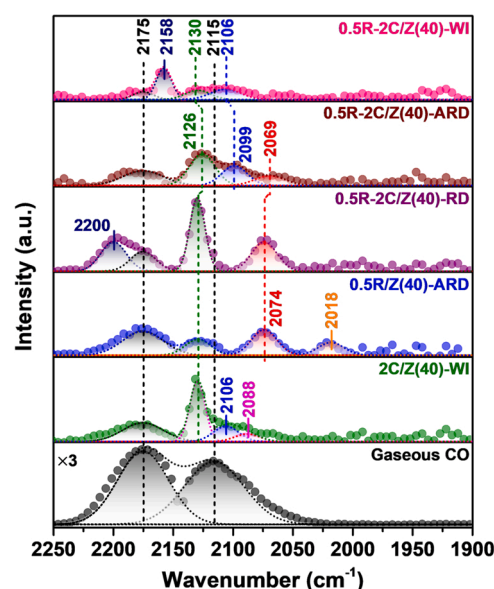


Fig. 6. CO-DRIFT profiles of the monometallic and bimetallic catalysts collected at 100 °C after N_2 flushing for 8 min.

metal [52]. Therefore, the low activation-energy barrier, facile spillover to the Ru–Cu interfacial site, and strong H-atom adsorption make Cu_1Ru highly promising for hydrogenation and hydrogenolysis reactions.

To further understand the active sites of the catalysts, CO-DRIFT profiles were obtained, as shown in Fig. 6. The peak related to gaseous CO at 2175 cm^{-1} persisted after N_2 flushing for 8 min, while the peak at 2115 cm^{-1} disappeared for all catalysts (Fig. S20). In the spectrum of the 2 C/Z(40)–WI catalyst, the band at 2130 cm^{-1} is attributed to linearly adsorbed CO on Cu^+ [Cu^+-CO] [53], and the bands at 2106 and 2088 cm^{-1} are assigned to linearly adsorbed CO on the low-indexed Cu^0 (e.g., edge, kink, defect sites) and the high-indexed Cu^0 surface planes (e.g., terrace), respectively [Cu^0-CO] [53]. In the spectrum of 0.5R/Z(40)–ARD, the band at 2130 cm^{-1} is assigned to the tricarbonyl species adsorbed on isolated Ru^{n+} ions present on the oxidized Ru NPs [$(RuO)_xRu^{n+}(CO)_3$]; the band at 2074 cm^{-1} is assigned to multicarbonyl species that were linearly adsorbed on partially oxidized Ru^{n+} [$Ru^{n+}(CO)_x$]; and the band at 2018 cm^{-1} is attributed to linearly adsorbed CO on Ru^0 on high-energy defect sites and/or isolated Ru^0 species surrounded by RuO_x [Ru^0-CO] [54]. It is difficult to identify the bands at 2050–2150 cm^{-1} for bimetallic catalysts because of the overlap of the peaks related to the Cu and Ru sites. However, some characteristics of CO adsorption on bimetallic catalysts can be derived. For the 0.5R–2C/Z(40)–RD catalyst, the band at 2200 cm^{-1} is assigned to linearly adsorbed CO on Cu^{2+} [$Cu^{2+}-CO$] [53]. The absence of bands at 2106 and 2018 cm^{-1} indicates that metallic Cu^0 and Ru^0 were not present in the 0.5R–2C/Z(40)–RD catalyst, which agrees well with the XRD, XAS, and XPS results. For the 0.5R–2C/Z(40)–ARD catalyst, the [Cu^+-CO] band was red-shifted from 2106 to 2099 cm^{-1} because of electron transfer from Cu and Ru. In addition, the [Ru^0-CO] band at 2018 cm^{-1} , which was observed in the monometallic 0.5R/Z(40)–ARD, was not observed for the 0.5R–2C/Z(40)–ARD catalyst. When considering the presence of metallic Ru^0 NPs (as confirmed by XRD, XAS, and XPS analyses), the absence of the CO adsorption band on metallic Ru^0 implies the preferential adsorption of CO on the Cu nanodomains in the shell. As for 0.5R–2C/Z(40)–ARD, the [Ru^0-CO] band was not observed for 0.5R–2C/Z(40)–WI; considering the exposed Ru^0 NPs, the absence of this band is attributed to Cl poisoning. The new band at 2158 cm^{-1} in the spectrum of 0.5R–2C/Z(40)–WI is assigned to bi-carbonyl adsorption on the Cu^+ species [$Cu^+-(CO)_2$] [53].

Table 3Conversion and product yields over the various types of catalysts.^{a, b}

Entry	Feedstock	Catalyst	$X_{\text{feedstock}}^c$	Y^d (mol%)					MeOH loss (vol.%)	C balance ^e (%)
				MLU	GVL	MV	MPEA	others		
1	Cellulose	None	30.0	N.D. ^f	N.D.	N.D.	N.D.	17.5	26.7	65.0
2		Z(40)	58.0	40.5	N.D.	N.D.	N.D.	3.0	21.7	75.0
3		Z(15)	62.0	35.2	N.D.	N.D.	N.D.	8.6	26.7	70.8
4		Z(2.6)	68.4	28.9	N.D.	N.D.	N.D.	16.6	38.3	66.5
5		HZSM-5(40)	53.0	33.0	N.D.	N.D.	N.D.	3.5	23.3	68.9
6		H β (19)	63.8	34.7	N.D.	N.D.	N.D.	10.2	34.7	70.5
7		2 C/Z(40)-WI	70.0	53.3	N.D.	N.D.	N.D.	1.9	18.0	78.9
8		0.5 R/Z(40)-ARD	68.0	50.0	N.D.	N.D.	N.D.	1.5	16.7	75.8
9		0.5R-1 C/Z(40)-ARD	82.5	30.5	29.9	0.3	0.1	4.9	13.3	79.6
10		0.5R-2 C/Z(40)-ARD	90.0	15.1	49.8	3.9	0.5	3.2	15.0	80.6
11		0.5R-3 C/Z(40)-ARD	93.2	13.6	46.5	5.4	1.2	7.9	15.0	80.1
12		0.5R-2 C/Z(40)-WI	70.0	32.0	10.4	N.D.	N.D.	10.7	13.7	75.9
13		0.5R-2 C/Z(40)-RD	74.0	35.9	12.6	N.D.	N.D.	8.3	12.7	76.8
14		0.5R-2 C/Z(40)-ARD + NaCl	72.0	28.8	N.D.	N.D.	N.D.	24.1	13.3	73.5
15		0.5R-2 C/Z(15)-ARD	87.0	19.5	24.8	0.8	1.1	10.5	25.0	65.2
16		0.5R-2 C/Z(2.6)-ARD	85.0	22.8	18.3	N.D.	N.D.	10.3	20.0	60.5
17		0.5R-2 C/ γ -Al ₂ O ₃ -ARD	35.0	N.D.	N.D.	N.D.	N.D.	18.2	10.0	52.0
18		0.5R-2 C/PS-ARD	30.0	N.D.	N.D.	N.D.	N.D.	13.5	8.3	45.0
19	Cellobiose	0.5R-2 C/Z(40)-ARD	92.5	7.8	57.4	5.2	2.3	4.3	16.0	83.2
20	Sucrose		94.0	9.6	56.8	4.8	3.6	3.7	16.7	83.5
21	Glucose		96.8	3.5	60.2	8.4	6.5	2.9	17.7	84.2
22	Fructose		100	1.7	66.8	12.6	3.2	2.5	19.3	86.8
23	5-HMF		100	N.D.	72.0	17.1	2.1	2.8	16.7	94.0
24	MLU		100	N.D.	N.D.	93.2	N.D.	5.3	21.7	98.5

^a MLU = methyl levulinate; GVL = γ -valerolactone; MV = methyl valerate; MPEA = methyl 3-pentanoate; others include cyclopentanone, 2,5-hexanedione, 5-methoxy methyl furfural, methyl D-glucopyranoside and pentanol.

^b Reaction conditions: 2 g of feedstock, 0.5 g of catalyst, 30 mL of methanol, 250 °C, initial H₂ pressure of 3 MPa, 5 h.

^c $X_{\text{feedstock}}$ = conversion of feedstock (Eq. (S1)).

^d Y = yield of the product (Eq. (S2)).

^e Carbon balance (Eq. (S3)).

^f N.D. = not detected.

2.2. Catalyst performance

One-pot direct conversion of cellulose to GVL was tested over various types of catalysts, and the results are listed in Table 3 and standard deviation presented in the Table S4. In the absence of a catalyst, the C–C and C–O bonds in the cellulose chain are cleaved to some extent in supercritical methanol, resulting in MDG, D-allose, methyl D-lyxofuranoside, and methyl D-ribosepyranoside formation (Fig. S21). In addition, low-molecular-weight cellulose-decomposed species, such as 1-methoxy 2-propanone and 1,1,2-trimethoxy ethane, were observed. The liquid product was dark brown, indicating the formation of humins or other polymeric species. When the Si/Al ratio in zeolite Y increased from 2.6 to 40, the MLU yield increased from 28.9% to 40.5%, indicating that an increase in the number of LASs is favorable for the formation of the MLU intermediate. Cellulose conversion over HZSM-5(40) and H β (40) resulted in lower MLU yields of 33.0% and 34.7%, respectively, compared to that over Z(40) (Table 3). In addition, the color of the liquids produced over HZSM-5(40) and H β (40) was darker than that over Z(40) (Fig. S22). The larger pore size of zeolite Y compared to those of HZSM-5 and H β (Fig. S23) allows large intermediates to easily penetrate its pores, which could result in a higher MLU yield. The selective production of MLU from cellulose over zeolite Y in supercritical methanol indicates that several consecutive cascade reactions occurred: (1) alcoholysis of cellulose (cleavage of the β -1,4 glycosidic bond) to produce MDG over the BASs and LASs; (2) isomerization of MDG to produce MDFF over the LASs; (3) dehydration of MDFF to produce 5-MMF over the BASs; and (4) alcoholysis of 5-MMF to produce MLU over the LASs and BASs (Fig. 1).

The use of reduced 2C/Z(40)-WI and 0.5R/Z(40)-ARD increased the cellulose conversion to 70.0% and 68.0%, respectively, and increased the MLU yields to 53.3% and 50.0%, respectively, as compare to those over Z(40). The liquid product over the 2C/Z(40)-WI catalyst was transparent, and that over the 0.5R/Z(40)-ARD catalyst was light yellowish (Fig. S24).

The formation of GVL was observed over the bimetallic xR-yC/Z(40)-ARD catalysts with higher cellulose conversion than the mono-metallic 2 C/Z(40)-WI and 0.5 R/Z(40)-ARD catalysts. For example, over 0.5R-2 C/Z(40)-ARD, a high GVL yield of 49.8% was achieved at a cellulose conversion of 90.0%. The liquid product was transparent, indicating negligible humin formation (Fig. S25). Other products included MV, methyl 3-pentanoate (MPEA), 2,5-HDO, and CPO. Plausible pathways for the formation of these byproducts are shown in Fig. S1; MPEA could be produced by the ring-opening of GVL, and the subsequent hydrogenation of MPEA could produce MV. The formation of CPO can occur through an FFA pathway; conversion of the acyclic-keto form of MDFF to acyclic C5 arabinose and subsequent dehydration can produce FFA [55]. Hydrogenation of FFA then produces FOL, which further undergoes acid-catalyzed Piancatelli rearrangement to yield 4-hydroxy-2-cyclopentenone (4-HCP). Subsequently, 4-HCP undergoes hydrogenation followed by dihydroxylation to produce CPO [56]. Further, 2,5-HDO can be produced by the hydrogenolysis of 5-MMF to 5-MF, hydrogenation of 5-MF to 5-MFA, followed by hydrogenolysis to 2,5-DMF, and subsequent hydrolysis of 2,5-DMF [51]. When the Cu loading was increased to 3 wt% in 0.5R-yC/Z(40)-ARD, the GVL yield slightly decreased to 46.5%, while the yields of MV and MPEA increased.

When 0.5R-2C/Z(40)-RD was used, cellulose conversion decreased to 74.0%, and the conversion of MLU to GVL was lower than that of 0.5R-2C/Z(40)-ARD. As shown in Fig. S26b, an unconverted 5-MMF intermediate was observed in the liquid product produced using 0.5R-2C/Z(40)-RD. Therefore, the low yield of GVL could be attributed to the incomplete reduction of Cu and Ru oxides to their metallic phase. The use of 0.5R-2C/Z(40)-WI resulted in a cellulose conversion of 70%, but the GVL yield was low (10.4%) because of the low activity for the conversion of MLU to GVL. One plausible reason for the low GVL yield could be Cl⁻ poisoning of the metallic sites [24,45,50]. As discussed in the previous section, the presence of Cl⁻ ions on the catalyst surface

suppresses dissociative H_2 adsorption. To further understand the role of Cl^- ions on the reactivity of the catalyst, 0.05 M NaCl was added to the reaction mixture containing 0.5R-2C/Z(40)-ARD. The cellulose conversion was 72.0% with a 28.8% yield of MLU; however, GVL was not detected. In addition, a high degree of humin formation occurred during the reaction owing to the condensation of 5-MMF and FFA (Fig. S27). Thus, the presence of Cl^- has a detrimental effect on cellulose conversion.

To examine the effect of the acidity of zeolite Y, cellulose conversion was conducted over 0.5R-2C/Z(z)-ARD catalysts with various Si/Al ratios. As the Si/Al ratio decreased from 40 to 2.6 (and thus the L/B ratio decreased from 3.92 to 1.12; Fig. S13b), the cellulose conversion and GVL yield decreased from 90.0% to 85.0% and from 49.8% to 18.3%, respectively, while the MLU yield increased from 15.1% to 22.8%. Thus, the high L/B ratio of the 0.5R-2C/Z(z)-ARD catalysts is beneficial for increasing the GVL yield. The cellulose conversion increased with decreasing Si/Al ratio of zeolite Y (z) (and thus with increasing L/B ratio; Fig. S13a) prior to metal loading (entries 2–4, Table 3), and the cellulose conversion decreased with decreasing L/B ratio of 0.5R-2C/Z(z)-ARD. These observations imply that the conversion of MLU to GVL occurred over the LASs and humin formation was more effectively suppressed compared to a catalyst rich in BASs [57] (Fig. S1) could shift the alcoholysis reaction forward. To further investigate the role of the acid sites in zeolite Y, PS [25] and $\gamma-Al_2O_3$ were used as supports. Over the 0.5R-2C/ $\gamma-Al_2O_3$ -ARD catalyst, very low cellulose conversion (35.0%) with 1,2 propanediol as the major product was observed due to the absence of BASs in $\gamma-Al_2O_3$ [58]. The absence of acid sites in 0.5R-2C/PS(40)-ARD resulted in a very low cellulose conversion of 30.0%. Therefore, the balance between BASs and LASs in zeolite Y and the facilitated dissociated H_2 adsorption on the core-shell Cu-Ru NPs play a critical role in the direct conversion of cellulose to GVL.

To understand the reaction mechanisms, disaccharides (cellobiose and sucrose), monosaccharides (glucose and fructose), and reaction intermediates (5-hydroxymethyl furfural (5-HMF), and MLU) were tested over the 0.5R-2C/Z(40)-ARD catalyst (Table 3). As the feedstock changed in the direction of the final GVL product in the reaction pathway (disaccharides \rightarrow monosaccharides \rightarrow 5-HMF), the GVL yield increased to 72.0%. The reaction intermediates and side products in the conversion of glucose and 5-HMF were similar to those in cellulose conversion (Fig. S28). GVL was not detected in the reaction mixture when MLU was used as the feedstock; however, MV was produced with high yield. The ring-opening of GVL to MPEA and subsequent hydrogenation of MPEA to MV could be activated at a high temperature of 250 °C. When a lower temperature was used (130 °C), MLU was converted to GVL with high yield (90%).

2.3. Optimization of the reaction conditions in supercritical methanol

The cellulose conversion and GVL yield were optimized by varying the reaction conditions over the 0.5R-2C/Z(40)-ARD catalyst. As the temperature increased from 220 to 250 °C, the cellulose conversion increased from 65.0% to 90.0% and the GVL yield increased from 10.2% to 49.8%, respectively, at the expense of MLU (Fig. S29a). A further increase in the temperature to 260 °C resulted in a slight increase in the cellulose conversion to 93%, but the GVL yield decreased to 45% because of the formation of MV via ring-opening of GVL followed by hydrogenation.

The time evolution of reaction monitored at 250 °C (Fig. S29b). As the reaction time increased to 5 h, a progressive increase in cellulose conversion and GVL yield with decreasing MLU yield was observed. When the reaction time was extended to 6 h, the cellulose conversion further increased to 94.0%, but the GVL yield decreased to 44.3% because of MV formation.

The effect of pressure on the cellulose conversion and product yield is presented in Fig. S29c. At low H_2 pressures in the range of 1–2 MPa, the cellulose conversion was 65.0–83.0% and the GVL yield was

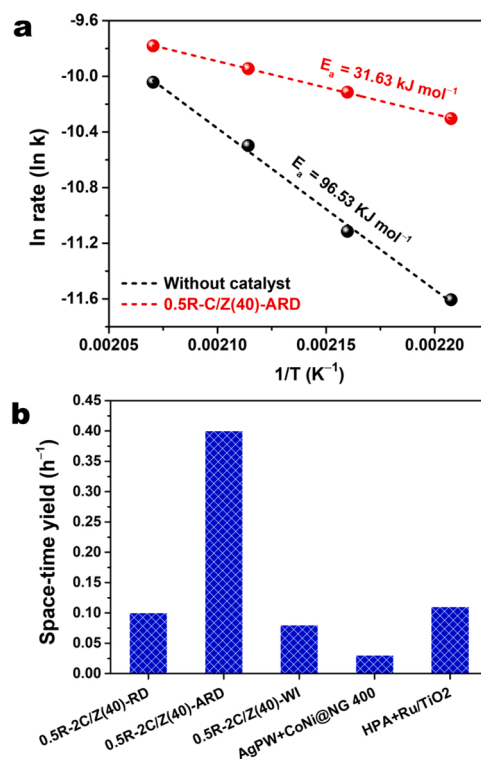


Fig. 7. (a) Arrhenius plots without catalyst and with 0.5R-2C/Z(40)-ARD catalyst. Reaction conditions for Arrhenius plot: 2 g of cellulose, 0.1 g of 0.5R-2C/Z(40)-ARD, 30 mL of methanol, and initial H_2 pressure of 1.0 MPa. (b) Comparison of space-time yields of various catalysts. Reaction conditions for STY: 2 g of cellulose, 0.5 g of catalyst, 30 mL of methanol, 250 °C, initial H_2 pressure of 3.0 MPa, and 5 h reaction time.

25.0–43.4%. At high H_2 pressure (4 MPa), the cellulose conversion increased to 95.0%, but the GVL yield decreased to 43.2% because of enhanced MV formation.

Based on the reaction data presented in Table S5 at low-to-medium conversions of 2.0–25%, the activation energies for cellulose conversion were calculated (Fig. 7a). The activation energy over the 0.5R-2C/Z(40)-ARD catalyst was approximately three times lower (31.6 kJ mol⁻¹) than that of the reaction without the catalyst (96.5 kJ mol⁻¹). In addition, the activation energy using 0.5R-2C/Z(40)-ARD was lower than those previously reported for cellulose conversion; for example, cellulose hydrolysis with dilute inorganic acid, 170–180 kJ mol⁻¹ [59]; cellulose hydrolysis with formic acid and HCl, 106 kJ mol⁻¹ [60]; cellulose hydrolysis with chloromethyl polystyrene functionalized with SO_3H , 83.0 kJ mol⁻¹ [61]; and cellulose hydrolysis and alcoholysis with $Al_2(SO_4)_3$, 165.8 and 183.5 kJ mol⁻¹ [62].

To further examine catalyst performance, the space-time yield (STY) was calculated as follows:

$$STY \text{ (h}^{-1}\text{)} = \frac{GVL \text{ produced (g)}}{catalyst \text{ weight (g)} \times reaction \text{ time (h)}} \quad (4)$$

As shown in Fig. 7b, the STY obtained using the 0.5R-2C/Z(40)-ARD catalyst was approximately 4–5 times larger than that obtained using 0.5R-2C/Z(40)-WI or 0.5R-2C/Z(40)-RD. In addition, the STY value obtained using 0.5R-2C/Z(40)-ARD was higher (0.40 h⁻¹) than those of previous cellulose-to-GVL works (AgPW + CoNi@NG400, 0.03 h⁻¹ [5]; HPA + Ru/TiO₂, 0.11 h⁻¹ [3] at the reaction temperature 200 and 150 °C, respectively). The high STY value, low activation energy, and high GVL yield demonstrate that 0.5R-2C/Z(40)-ARD is highly promising for the one-pot conversion of cellulose to GVL.

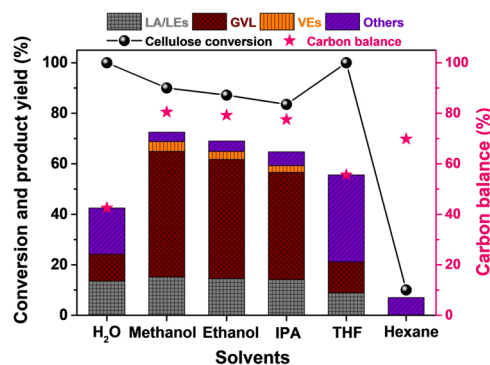


Fig. 8. Effect of solvent on the conversion of cellulose over the 0.5R-2C/Z(40)-ARD catalyst. Reaction conditions: 2 g of cellulose, 0.5 g of catalyst, 30 mL of solvent, 250 °C, initial H₂ pressure of 3.0 MPa, and 5 h reaction time.

2.4. Effect of solvent

The influence of the solvent on the biomass conversion and selectivity of targeted products is a critical issue, because many side reactions can occur in different reaction media [63,64]. In this study, to investigate the solvent effect, representative solvents including highly polar protic (water), moderately polar protic (methanol, ethanol, IPA), polar aprotic (THF), and nonpolar (n-hexane) solvents were chosen for the conversion of cellulose at 250 °C for 5 h with a 3.0 MPa initial H₂ pressure. When water was used as the reaction medium, the GVL yield was very low (11.0%, Fig. 8). The other products included unconverted sugars (e.g., glucose and fructose) and acidic species (e.g., acetic acid and lactic acid) (Fig. S30a). In addition, humin formation is facilitated in a highly protic environment [65]. The cellulose conversion and product selectivity were similar when moderately polar alcoholic solvents were used. The GVL yield decreased slightly from 49.8% to 42.5% as the number of carbons in the alcohols increased from one to three. A small degree of humin formation was observed in IPA (Fig. S30d); this could be due to easy proton transfer from the secondary alcohol to 5-HMF or other reactive intermediates. When THF solvent was used, the GVL yield was significantly lower (12.4%), while side products, such as 2,5-DMF, 2-pentanone, 2-hexanone, CPO, LA, isosorbide, and hydroquinone, were produced (Fig. S30e). The color of the reaction mixture was dark, indicating that humin formation occurred extensively, probably due to the polymerization of furanic compounds with THF-derived decomposed furanic species [66]. When n-hexane was used, only a 10% conversion of cellulose was observed, which could be due to the low solubility of sugars and other oxygenated compounds in the nonpolar solvent. Therefore, methanol is the most suitable solvent for the conversion of cellulose to high-yield GVL.

2.5. Reaction mechanism

Based on the aforementioned results, a possible reaction pathway for the one-pot conversion of cellulose to GVL over the 0.5R-2C/Z(40)-ARD catalyst is proposed (Fig. S31): (1) alcoholysis of cellulose to MDG over the BASs and LASs; (2) isomerization of MDG to MDFF over the LASs; (3) dehydration of MDFF to 5-MMF over the BASs; (4) alcoholysis of 5-MMF to MLU over the LASs and BASs; (5) dealcoholization of MLU to α -AL over the BASs; and (6) hydrogenation of α -AL to GVL over the Cu-Ru metallic sites. Cellulose contains anhydro-glucose monomer units that are linked to each other via a β -1,4-glycosidic bond in a chair conformation. The alcoholysis of cellulose over the BASs and LASs of zeolite Y produces fragments of β -1,4-glucans, and further alcoholysis of the glycosidic bond yields MDG as a product [67]. The produced MDG undergoes isomerization over the LASs by an intramolecular hydride shift from the C2 carbon atom to the C1 carbon atom of the MDG. MDG and MDFF were detected in the product from the low cellulose conversion

(12.8%) under mild reaction conditions (180 °C, 1.0 MPa initial H₂ pressure for 1.0 h, Fig. S32a). Subsequently, the dehydration of the hemiacetal at C2 of MDFF results in the production of intermediate tertiary carbenium cations, which undergo two consecutive β -dehydration reactions, resulting in the formation of 5-HMF [68]. Subsequently, 5-HMF underwent methanolysis to form 5-MMF. In fact, 5-MMF was detected as the reaction product using zeolite Y (Fig. S22a). Furthermore, 5-MMF is converted to 5-HDMF via acetalization, and subsequent proton attack of 5-HDMF can produce MLU [67]. The presence of 5-HDMF was observed in the product yielded at low cellulose conversion (18.5%) and mild reaction conditions (190 °C, 1.0 MPa initial H₂ pressure for 1.5 h, Fig. S32b). In addition, a proton from the BASs of zeolite Y could attack the carbonyl group of MLU to form pseudo-MLU via intramolecular cyclization. Subsequently, pseudo-MLU undergoes dealcoholization to form α -AL via hydrogen release from the ring carbon and the dissociation of the -OCH₃ group [25]. The formation of α -AL as an intermediate was confirmed by the reaction products over the reduced 2C/Z(40)-WI catalyst (Fig. S24a). Subsequently, α -AL undergoes hydrogenation over Cu-Ru metallic sites via weakly bonded hydrogen atoms to produce GVL.

2.6. Recyclability

To investigate the stability and reusability of the 0.5R-2C/Z(40)-ARD catalyst, six consecutive cellulose conversion cycles were performed, and the results are shown in Fig. 9a. After the 1st run, the spent catalyst was separated from the reaction mixture via centrifugation. The collected catalyst was washed with methanol and water and then dried overnight in a vacuum oven at 80 °C. When the dried catalyst was used in the 2nd run without additional coke burning or activation, the cellulose conversion and GVL yield decreased from 90.0% to 70.0% and from 49.8% to 26.2%, respectively. There are several reasons for the decrease in the catalytic activity, including: the deposition of residual cellulose, reaction intermediates, and coke on the active sites; metal leaching; oxidation of the metal sites; and changes in the textural properties of the zeolite. To examine the deposition of methanol/water-insoluble organic species, TGA of the spent catalyst collected after the 1st run was performed under an air flow after the in situ removal of water or other volatile species in the TGA chamber (Fig. 9b). Weight loss of the spent catalyst started to occur near 150 °C, which was caused by the decomposition of the light organic fraction. The main decomposition of organic species occurred above 300 °C. The total amount of methanol insoluble organic species deposited on the spent catalyst was 15.4 wt%. The Cu and Ru contents in the fresh and spent catalysts, which were measured using ICP-OES, did not change significantly (Fig. 9c); thus, metal leaching did not occur during the reaction. Metal oxide phases, such as Cu₂O, CuO, and RuO₂, were not detected in the spent catalyst (Fig. 9d). As shown in Fig. 9e, a carbon layer with a thickness of 0.6–1.1 nm was deposited on the catalyst surface. The HAADF-STEM image and corresponding EDS images show that the core-shell structure of the Cu-Ru metal sites was maintained in the spent catalyst (Fig. 9f–j). After the reaction, the total number of acid sites in the spent catalyst decreased from 0.339 to 0.145 mmol g⁻¹ (Fig. 9k, Table 2). The pyridine-DRIFT profile of the spent catalyst showed that the number of LASs decreased, resulting in a lower L/B ratio of 2.71 than that of the fresh catalyst (3.92). After pre-oxidation at 450 °C, the H₂-TPR profiles of the spent catalyst were similar to those of the fresh catalyst (Fig. 9m). Therefore, considering all the results for the spent catalyst, organic layer deposition was the major source of the decrease in the activity of 0.5R-2C/Z(40)-ARD.

To regain the activity of the spent catalyst, the dried catalyst collected after the 1st run was calcined at 450 °C at a ramping rate of 2 °C min⁻¹ under an air flow of 30 mL min⁻¹ to burn the organic species deposited on the catalyst surface. Then, the catalyst was reduced at 450 °C for 2 h under a 5% H₂/Ar flow of 30 mL min⁻¹. The TGA profile, total acidity, and L/B ratio of the activated catalyst were similar to those of

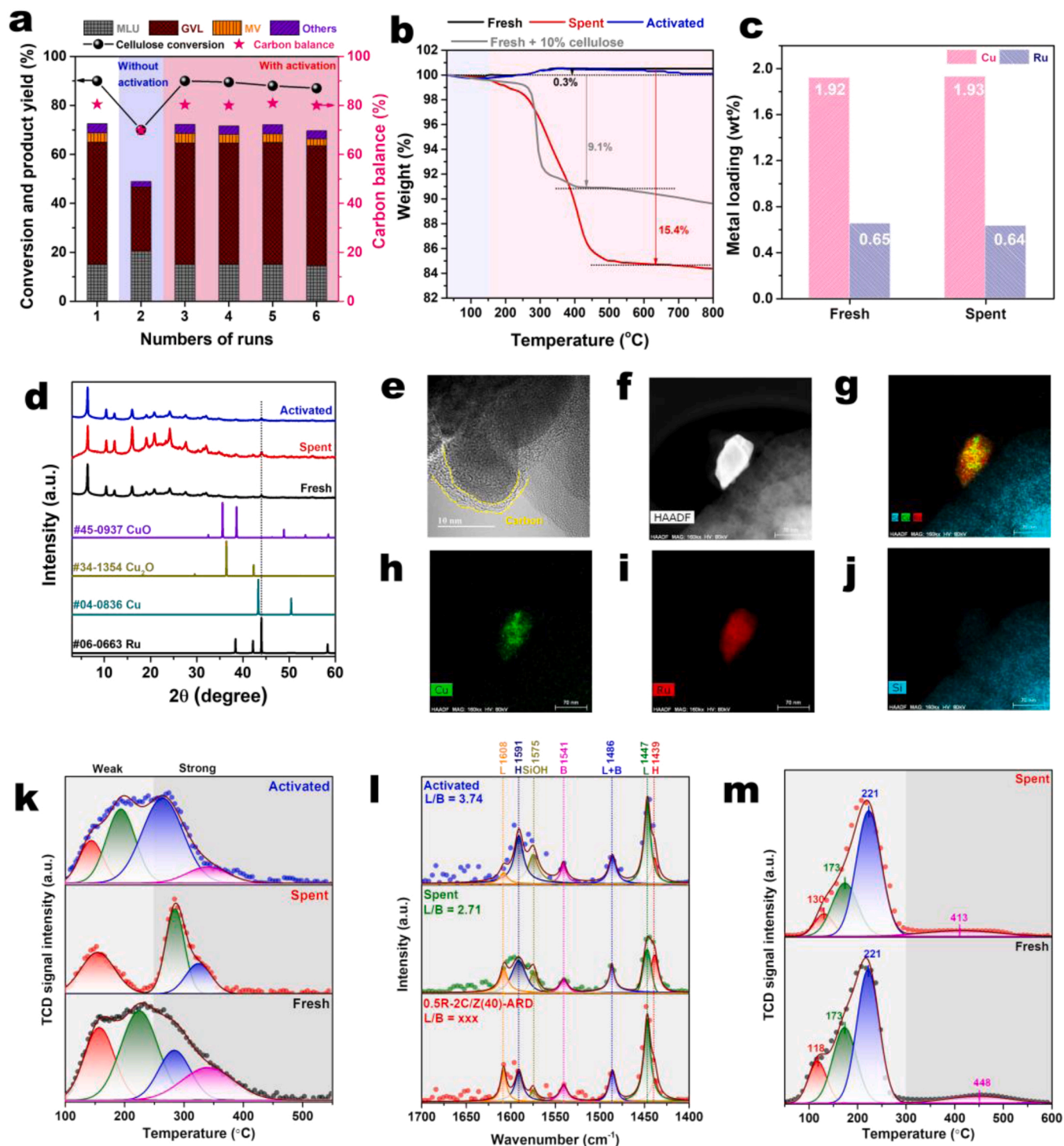


Fig. 9. (a) Reusability of the 0.5R-2C/Z(40)-ARD catalyst in the conversion of cellulose; reaction conditions: 2 g of cellulose, 0.5 g of catalyst, 30 mL of methanol, 250 °C, initial H₂ pressure of 3.0 MPa, and reaction time of 5 h. (b) TGA profiles, (d) XRD patterns, (k) NH₃-TPD profiles, and (i) pyridine-DRIFT profiles of the fresh, spent, and activated 0.5R-2C/Z(40)-ARD. (c) ICP-OES data and (m) H₂-TPR profiles of the fresh and spent 0.5R-2C/Z(40)-ARD. (e) HR-TEM image and (f-j), HAADF-STEM and corresponding EDS images of the spent 0.5R-2C/Z(40)-ARD.

the fresh catalyst (Fig. 9b and k-m, Table 2), indicating that complete combustion of the organic layer restores the activity of the active sites. The activated catalyst was reused under the same reaction conditions for the next four consecutive runs. After six runs, the cellulose conversion and GVL yield were similar to those of the fresh catalyst (Fig. 9a), indicating the high stability and reusability of the catalyst.

3. Conclusion

In this study, we demonstrated that the one-pot cascade conversion of cellulose over a bimetallic 0.5R-2C/Z(40)-ARD catalyst resulted in a high yield of GVL. Under supercritical methanol conditions at 250 °C, 3 MPa initial H₂ pressure, and 5 h reaction time, cellulose conversion was 90%, with a GVL yield of 49.8%. The balanced LASs and BASs of the 0.5R-2C/Z(40)-ARD catalyst effectively converted cellulose to MDG by

alcoholysis, MDG to MDFF by isomerization, MDFF to 5-HDMF by consecutive dealcoholization and dehydration, and 5-HDMF to MLU by alcoholysis. The geometry of the Cu nanodomains deposited on the Ru NPs facilitated dissociative H₂ adsorption on the bimetallic sites, which increased the hydrogenation activity of MLU to GVL. The performance of the ARD catalyst was compared to that of the conventional RD and WI methods. Because of the suppressed activity of acid sites of zeolite Y and residual Cl⁻ ions on the metallic sites, 0.5R–2C/Z(40)–WI had a low GVL yield of 10.4%. In the case of 0.5R–2C/Z(40)–RD, the incomplete reduction of metallic sites and suppressed acid sites resulted in a low GVL yield of 12.6%. The use of water, THF, and hexane resulted in a low yield of GVL (0%–12.4%) and severe humin formation. The 0.5R–2C/Z(40)–ARD catalyst was used for up to six runs without loss of catalyst activity after a coke-burnout treatment. The one-pot conversion of cellulose to GVL over 0.5R–2C/Z(40)–ARD catalyst was achieved with high yield and suppression of coke formation. Therefore, this catalyst is highly promising for producing value-added chemicals directly from cellulose.

CRedit authorship contribution statement

Neha Karanwal: Conceptualization, Methodology, Formal analysis, Data curation, Writing – original draft. **Rizky Gilang Kurniawan:** Conceptualization, Methodology, Investigation, Software, Data curation. **Jaeyong Park:** Validation, Formal analysis, Investigation. **Deepak Verma:** Methodology, Formal analysis, Investigation. **Suryun Oh:** Data curation, Visualization. **Seung Min Kim:** Data curation, Visualization. **Sang Kyu Kwak:** Conceptualization, Methodology, Investigation. **Jaehoon Kim:** Supervision, Project administration, Resources, Writing – review & editing, Funding acquisition.

Declaration of Competing Interest

The authors declare that they have no known competing financial interests or personal relationships that could have appeared to influence the work reported in this paper.

Acknowledgments

This research was supported by the Bio & Medical Technology Development Program of the National Research Foundation (NRF) funded by the Korean government (MSIT) (No. 2022M3A9F3017700). Additional supports from the National Research Foundation of Korea grant funded by the Ministry of Science and ICT, Republic of Korea, are also acknowledged (Grant numbers 2020H1D3A2A02085762, and 2020R1C1C1003236). We used the 8C synchrotron beamline of the Pohang Acceleration Laboratory Korea under the contact no. 2022-1st-8C-033.

Appendix A. Supplementary material

Supplementary data associated with this article can be found in the online version at [doi:10.1016/j.apcatb.2022.121466](https://doi.org/10.1016/j.apcatb.2022.121466).

References

- [1] L.T. Mika, E. Csefalvay, A. Nemeth, Catalytic conversion of carbohydrates to initial platform chemicals: chemistry and sustainability, *Chem. Rev.* 118 (2018) 505–613, <https://doi.org/10.1021/acs.chemrev.7b00395>.
- [2] H. Heeres, R. Handana, D. Chunai, C.B. Rasrendra, B. Girisuta, H.J. Heeres, Combined dehydration/(transfer)-hydrogenation of C6-sugars (D-glucose and D-fructose) to γ -valerolactone using ruthenium catalysts, *Green Chem.* 11 (2009) 1247–1255, <https://doi.org/10.1039/B904693C>.
- [3] J. Cui, J. Tan, T. Deng, X. Cui, H. Zheng, Y. Zhu, Y. Li, Direct conversion of carbohydrates to γ -valerolactone facilitated by a solvent effect, *Green Chem.* 17 (2015) 3084–3089, <https://doi.org/10.1039/C5GC00110B>.
- [4] Y.B. Huang, T. Yang, Y.J. Luo, A.F. Liu, Y.H. Zhou, H. Pan, F. Wang, Simple and efficient conversion of cellulose to γ -valerolactone through an integrated alcoholysis/transfer hydrogenation system using Ru and aluminium sulfate catalysts, *Catal. Sci. Technol.* 8 (2018) 6252–6262, <https://doi.org/10.1039/C8CY01971A>.
- [5] S. Zhu, H. Liu, S. Wang, X. Gao, P. Wang, J. Wang, W. Fan, One-step efficient non-hydrogen conversion of cellulose into γ -valerolactone over AgPW/CoNi@ NG composite, *Appl. Catal. B* 284 (2021), 119698, <https://doi.org/10.1016/j.apcatb.2020.119698>.
- [6] I.T. Horváth, H. Mehdi, V. Fábos, L. Boda, L.T. Mika, γ -Valerolactone—a sustainable liquid for energy and carbon-based chemicals, *Green Chem.* 10 (2008) 238–242, <https://doi.org/10.1039/B712863K>.
- [7] J.S. Luterbacher, J.M. Rand, D.M. Alonso, J. Han, J.T. Youngquist, C.T. Maravelias, B.F. Pfeiffer, J.A. Dumesic, Nonenzymatic sugar production from biomass using biomass-derived γ -valerolactone, *Science* 343 (2014) 277–280, <https://doi.org/10.1126/science.1246748>.
- [8] J.Q. Bond, D.M. Alonso, D. Wang, R.M. West, J.A. Dumesic, Integrated catalytic conversion of γ -valerolactone to liquid alkenes for transportation fuels, *Science* 327 (2010) 1110–1114, <https://doi.org/10.1126/science.1184362>.
- [9] F. Liguori, C. Moreno-Marroan, P. Barbaro, Environmentally friendly synthesis of γ -valerolactone by direct catalytic conversion of renewable sources, *ACS Catal.* 5 (2015) 1882–1894, <https://doi.org/10.1021/cs501922e>.
- [10] N. Karanwal, M.G. Sibi, M.K. Khan, A.A. Myint, B. Chan Ryu, J.W. Kang, J. Kim, Trimetallic Cu–Ni–Zn/H-ZSM-5 catalyst for the one-pot conversion of levulinic acid to high-yield 1, 4-pentanediol under mild conditions in an aqueous medium, *ACS Catal.* 11 (2021) 2846–2864, <https://doi.org/10.1021/acscatal.0c04216>.
- [11] S. Dutta, I.K. Yu, D.C. Tsang, Y.H. Ng, Y.S. Ok, J. Sherwood, J.H. Clark, Green synthesis of gamma-valerolactone (GVL) through hydrogenation of biomass-derived levulinic acid using non-noble metal catalysts: a critical review, *Chem. Eng. J.* 372 (2019) 992–1006, <https://doi.org/10.1016/j.cej.2019.04.199>.
- [12] S. Song, L. Di, G. Wu, W. Dai, N. Guan, L. Li, Meso-Zr-Al-beta zeolite as a robust catalyst for cascade reactions in biomass valorization, *Appl. Catal. B* 205 (2017) 393–403, <https://doi.org/10.1016/j.apcatb.2016.12.056>.
- [13] H. Li, Z. Fang, S. Yang, Direct conversion of sugars and ethyl levulinate into γ -valerolactone with superparamagnetic acid–base bifunctional ZrFeO x nanocatalysts, *ACS Sustain. Chem. Eng.* 4 (2016) 236–246, <https://doi.org/10.1021/acssuschemeng.5b01480>.
- [14] B. Sarkar, W. Kwek, D. Verma, J. Kim, Effective vacuum residue upgrading using sacrificial nickel (II) dimethylglyoxime complex in supercritical methanol, *Appl. Catal. A* 545 (2017) 148–158, <https://doi.org/10.1016/j.apcata.2017.07.033>.
- [15] S. Grundner, W. Luo, M. Sanchez-Sanchez, J.A. Lercher, Synthesis of single-site copper catalysts for methane partial oxidation, *Chem. Commun.* 52 (2016) 2553–2556, <https://doi.org/10.1039/C5CC08371K>.
- [16] G.J. Hutchings, J.C. Védrine, *Heterogeneous Catalyst Preparation*, Springer, 2004, https://doi.org/10.1007/978-3-662-05981-4_6.
- [17] W. Depmeier, *Introduction and Structure*, 2002, <https://doi.org/10.1002/9783527618286.ch18>.
- [18] F. Bottomley, Some reactions of hydrazine with ruthenium compounds, *Can. J. Chem.* 48 (1970) 351–355, <https://doi.org/10.1139/v70-052>.
- [19] A.D. Allen, F. Bottomley, R.O. Harris, V. Reinsalu, C. Senoff, Ruthenium complexes containing molecular nitrogen, *J. Am. Chem. Soc.* 89 (1967) 5595–5599, <https://doi.org/10.1021/ja00998a016>.
- [20] T. Kon'kova, A. Rysev, Inversion of montmorillonite ion-exchange characteristics, *Colloid J.* 82 (2020) 130–135, <https://doi.org/10.1134/S1061933X20020064>.
- [21] A.G. Shastri, J. Schwank, The influence of hydrazine reduction on metal dispersion and support morphology in bimetallic Ru–Au/MgO catalysts, *J. Catal.* 98 (1986) 191–203, [https://doi.org/10.1016/0021-9517\(86\)90308-8](https://doi.org/10.1016/0021-9517(86)90308-8).
- [22] C. Ducamp-Sangués, R. Herrera-Urbina, M. Figlarz, Fine palladium powders of uniform particle size and shape produced in ethylene glycol, *Solid State Ion.* 63 (1993) 25–30, [https://doi.org/10.1016/0167-2738\(93\)90081-D](https://doi.org/10.1016/0167-2738(93)90081-D).
- [23] B. Lin, R. Wang, J. Lin, S. Du, X. Yu, K. Wei, Preparation of chlorine-free alumina-supported ruthenium catalyst for ammonia synthesis base on RuCl₃ by hydrazine reduction, *Catal. Commun.* 8 (2007) 1838–1842, <https://doi.org/10.1016/j.catcom.2007.02.021>.
- [24] R. Inyanyi, A.F. Barus, R. Gunawan, J. Park, G.T. Jaya, H.S. Cahyadi, M.G. Sibi, S. K. Kwak, D. Verma, J. Kim, RuO₂–Ru/H β zeolite catalyst for high-yield direct conversion of xylose to tetrahydrofurfuryl alcohol, *Appl. Catal. B* 291 (2021), 120120, <https://doi.org/10.1016/j.apcatb.2021.120120>.
- [25] N. Karanwal, D. Verma, P. Butolia, S.M. Kim, J. Kim, One-pot direct conversion of levulinic acid into high-yield valeric acid over a highly stable bimetallic Nb–Cu/Zr-doped porous silica catalyst, *Green Chem.* 22 (2020) 766–787, <https://doi.org/10.1039/C9GC03516H>.
- [26] J. Song, Y. Wang, E.D. Walter, N.M. Washton, D. Mei, L. Kovarik, M.H. Engelhard, S. Proding, Y. Wang, C.H. Peden, F. Gao, Toward rational design of Cu/SSZ-13 selective catalytic reduction catalysts: implications from atomic-level understanding of hydrothermal stability, *ACS Catal.* 7 (2017) 8214–8227, <https://doi.org/10.1021/acscatal.7b03020>.
- [27] L. Meda, G. Ranghino, G. Moretti, G. Cerofolini, XPS detection of some redox phenomena in Cu-zeolites, *Surf. Interface Anal.* 33 (2002) 516–521, <https://doi.org/10.1002/sia.1228>.
- [28] A.K. Sharma, S.K. Gupta, Surface characterization of copper-silicon catalysts, *J. Catal.* 93 (1985) 68–74, [https://doi.org/10.1016/0021-9517\(85\)90151-4](https://doi.org/10.1016/0021-9517(85)90151-4).
- [29] J. Shen, A. Adnot, S. Kaliaguine, An ESCA study of the interaction of oxygen with the surface of ruthenium, *Appl. Surf. Sci.* 51 (1991) 47–60, [https://doi.org/10.1016/0169-4332\(91\)90061-N](https://doi.org/10.1016/0169-4332(91)90061-N).
- [30] Y.I. Kim, W.E. Hatfield, Electrical, magnetic and spectroscopic properties of tetraethiafulvalene charge transfer compounds with iron, ruthenium, rhodium and iridium halides, *Inorg. Chim. Acta* 188 (1991) 15–24, [https://doi.org/10.1016/S0020-1693\(00\)80911-1](https://doi.org/10.1016/S0020-1693(00)80911-1).

- [31] L.S. Kau, D.J. Spira-Solomon, J.E. Penner-Hahn, K.O. Hodgson, E.I. Solomon, X-ray absorption edge determination of the oxidation state and coordination number of copper. Application to the type 3 site in *Rhus vernicifera* laccase and its reaction with oxygen, *J. Am. Chem. Soc.* 109 (1987) 6433–6442, <https://doi.org/10.1021/ja00255a032>.
- [32] L.S. Kau, K.O. Hodgson, E.I. Solomon, X-ray absorption edge and EXAFS study of the copper sites in zinc oxide methanol synthesis catalysts, *J. Am. Chem. Soc.* 111 (1989) 7103–7109, <https://doi.org/10.1021/ja00200a032>.
- [33] S.E. Shadle, J.E. Penner-Hahn, H.J. Schugar, B. Hedman, K.O. Hodgson, E. I. Solomon, X-ray absorption spectroscopic studies of the blue copper site: metal and ligand K-edge studies to probe the origin of the EPR hyperfine splitting in plastocyanin, *J. Am. Chem. Soc.* 115 (1993) 767–776, <https://doi.org/10.1021/ja00055a057>.
- [34] Y. Okamoto, T. Kubota, H. Gotoh, Y. Ohto, H. Aritani, T. Tanaka, S. Yoshida, XAFS study of zirconia-supported copper catalysts for the NO–CO reaction: deactivation, rejuvenation and stabilization of Cu species, *J. Chem. Soc. Faraday Trans. 94* (1998) 3743–3752, <https://doi.org/10.1039/A807152G>.
- [35] G. Meitzner, G. Via, F. Lytle, J. Sinfelt, Structure of bimetallic clusters. Extended x-ray absorption fine structure (EXAFS) studies of Ru–Cu clusters, *J. Chem. Phys.* 72 (1980) 4832–4844, <https://doi.org/10.1063/1.444789>.
- [36] J.H. Sinfelt, Y. Lam, J. Cusumano, A. Barnett, Nature of ruthenium-copper catalysts, *J. Catal.* 42 (1976) 227–237, [https://doi.org/10.1016/0021-9517\(76\)90257-8](https://doi.org/10.1016/0021-9517(76)90257-8).
- [37] H. Okamoto, Cu–Ru (copper-ruthenium), *J. Phase Equilib.* 13 (1992), <https://doi.org/10.1007/BF02674997>, 440–440.
- [38] H.G. Karge, V. Dondur, J. Weitkamp, Investigation of the distribution of acidity strength in zeolites by temperature-programmed desorption of probe molecules. 2. Dealuminated Y-type zeolites, *J. Phys. Chem.* 95 (1991) 283–288, <https://doi.org/10.1021/j100154a053>.
- [39] F. Yi, Y. Chen, Z. Tao, C. Hu, X. Yi, A. Zheng, X. Wen, Y. Yun, Y. Yang, Y. Li, Origin of weak Lewis acids on silanol nests in dealuminated zeolite Beta, *J. Catal.* 380 (2019) 204–214, <https://doi.org/10.1016/j.jcat.2019.10.008>.
- [40] A. Clemens, A. Shishkin, P.-A. Carlsson, M. Skoglundh, F. Martínez-Casado, Z. Matej, O. Balmes, H. Harelind, Reaction-driven ion exchange of copper into zeolite SSZ-13, *ACS Catal.* 5 (2015) 6209–6218, <https://doi.org/10.1021/acscatal.5b01200>.
- [41] F. Benaliouche, Y. Boucheffa, P. Ayrault, S. Mignard, P. Magnoux, NH₃-TPD and FTIR spectroscopy of pyridine adsorption studies for characterization of Ag- and Cu-exchanged X zeolites, *Microporous Mesoporous Mater.* 111 (2008) 80–88, <https://doi.org/10.1016/j.micromeso.2007.07.006>.
- [42] I. Khalil, C.M. Celis-Cornejo, K. Thomas, P. Bazin, A. Traver, D.J. Perez-Martinez, V.G. Baldovino-Medrano, J.-F. Paul, F. Maugé, In situ IR-ATR study of the interaction of nitrogen heteroaromatic compounds with HY zeolites: experimental and theoretical approaches, *ChemCatChem* 12 (2020) 1095–1108, <https://doi.org/10.1002/cctc.201901560>.
- [43] I. Graça, M. Bacariza, A. Fernandes, D. Chadwick, Desilicated NaY zeolites impregnated with magnesium as catalysts for glucose isomerisation into fructose, *Appl. Catal. B* 224 (2018) 660–670, <https://doi.org/10.1016/j.apcatb.2017.11.009>.
- [44] M. Richter, M. Fait, R. Eckelt, E. Schreier, M. Schneider, M.-M. Pohl, R. Fricke, Oxidative gas phase carbonylation of methanol to dimethyl carbonate over chloride-free Cu-impregnated zeolite Y catalysts at elevated pressure, *Appl. Catal. B* 73 (2007) 269–281, <https://doi.org/10.1016/j.apcatb.2006.11.015>.
- [45] D.A. Echeverri, J.M. Marín, G.M. Restrepo, L.A. Rios, Characterization and carbonylic hydrogenation of methyl oleate over Ru–Sn/Al₂O₃: effects of metal precursor and chlorine removal, *Appl. Catal. A* 366 (2009) 342–347, <https://doi.org/10.1016/j.apcata.2009.07.029>.
- [46] J. Li, M. Kitano, T.N. Ye, M. Sasase, T. Yokoyama, H. Hosono, Chlorine-tolerant ruthenium catalyst derived using the unique anion-exchange properties of 12 CaO·7 Al₂O₃ for ammonia synthesis, *ChemCatChem* 9 (2017) 3078–3083, <https://doi.org/10.1002/cctc.201700353>.
- [47] G. Kyriakou, M.B. Boucher, A.D. Jewell, E.A. Lewis, T.J. Lawton, A.E. Baber, H. L. Tierney, M. Flytzani-Stephanopoulos, E.C.H. Sykes, Isolated metal atom geometries as a strategy for selective heterogeneous hydrogenations, *Science* 335 (2012) 1209–1212, <https://doi.org/10.1126/science.1215864>.
- [48] K. Mudiysanase, Y. Yang, F.M. Hoffmann, O.J. Furlong, J. Hrbek, M.G. White, P. Liu, D.J. Stacchiola, Adsorption of hydrogen on the surface and sub-surface of Cu (111), *J. Chem. Phys.* 139 (2013), 044712, <https://doi.org/10.1063/1.4816515>.
- [49] M. Chou, J.R. Chelikowsky, Theoretical study of hydrogen adsorption on Ru (0001): possible surface and subsurface occupation sites, *Phys. Rev. B* 39 (1989) 5623, <https://doi.org/10.1103/PhysRevB.39.5623>.
- [50] S. Murata, K.I. Aika, Removal of chlorine ions from Ru/MgO catalysts for ammonia synthesis, *Appl. Catal. A* 82 (1992) 1–12, [https://doi.org/10.1016/0926-860X\(92\)80001-S](https://doi.org/10.1016/0926-860X(92)80001-S).
- [51] R. Gunawan, H.S. Cahyadi, R. Insyani, S.K. Kwak, J. Kim, Density functional theory investigation of the conversion of 5-(hydroxymethyl) furfural into 2, 5-dimethyl-furan over the Pd (111), Cu (111), and Cu₃Pd (111) surfaces, *J. Phys. Chem. C* (2021), <https://doi.org/10.1021/acs.jpcc.0c10639>.
- [52] B. Hammer, J.K. Norskov, Why gold is the noblest of all the metals, *Nature* 376 (1995) 238–240, <https://doi.org/10.1038/376238a0>.
- [53] K. Hadjiivanov, H. Knözinger, FTIR study of CO and NO adsorption and coadsorption on a Cu/SiO₂ catalyst: probing the oxidation state of copper, *Phys. Chem. Chem. Phys.* 3 (2001) 1132–1137, <https://doi.org/10.1039/B009649K>.
- [54] S.Y. Chin, C.T. Williams, M.D. Amiridis, FTIR studies of CO adsorption on Al₂O₃- and SiO₂-supported Ru catalysts, *J. Phys. Chem. B* 110 (2006) 871–882, <https://doi.org/10.1021/jp053908q>.
- [55] L. Zhang, G. Xi, Z. Chen, D. Jiang, H. Yu, X. Wang, Highly selective conversion of glucose into furfural over modified zeolites, *Chem. Eng. J.* 307 (2017) 868–876, <https://doi.org/10.1016/j.cej.2016.09.001>.
- [56] M. Hronec, K. Fulajtarova, T. Soták, Highly selective rearrangement of furfuryl alcohol to cyclopentanone, *Appl. Catal. B* 154 (2014) 294–300, <https://doi.org/10.1016/j.apcatb.2014.02.029>.
- [57] T.D. Swift, H. Nguyen, Z. Erdman, J.S. Kruger, V. Nikolakis, D.G. Vlachos, Tandem Lewis acid/Bronsted acid-catalyzed conversion of carbohydrates to 5-hydroxymethylfurfural using zeolite beta, *J. Catal.* 333 (2016) 149–161, <https://doi.org/10.1016/j.jcat.2015.10.009>.
- [58] C. Liu, C. Zhang, S. Hao, S. Sun, K. Liu, J. Xu, Y. Zhu, Y. Li, WO_x modified Cu/Al₂O₃ as a high-performance catalyst for the hydrogenolysis of glucose to 1, 2-propanediol, *Catal. Today* 261 (2016) 116–127, <https://doi.org/10.1016/j.cattod.2015.06.030>.
- [59] B. Girisuta, L. Janssen, H. Heeres, Kinetic study on the acid-catalyzed hydrolysis of cellulose to levulinic acid, *Ind. Eng. Chem. Res.* 46 (2007) 1696–1708, <https://doi.org/10.1021/ie061186z>.
- [60] Y. Sun, J. Zhuang, L. Lin, P. Ouyang, Clean conversion of cellulose into fermentable glucose, *Biotechnol. Adv.* 27 (2009) 625–632, <https://doi.org/10.1016/j.biotechadv.2009.04.023>.
- [61] Y.B. Huang, Y. Fu, Hydrolysis of cellulose to glucose by solid acid catalysts, *Green Chem.* 15 (2013) 1095–1111, <https://doi.org/10.1039/C3GC40136G>.
- [62] Y.B. Huang, T. Yang, Y.T. Lin, Y.Z. Zhu, L.C. Li, H. Pan, Facile and high-yield synthesis of methyl levulinate from cellulose, *Green Chem.* 20 (2018) 1323–1334, <https://doi.org/10.1039/C7GC02883K>.
- [63] M.A. Mellmer, C. Sener, J.M.R. Gallo, J.S. Luterbacher, D.M. Alonso, J.A. Dumesic, Solvent effects in acid-catalyzed biomass conversion reactions, *Angew. Chem. Int. Ed.* 53 (2014) 11872–11875, <https://doi.org/10.1002/anie.201408359>.
- [64] T.W. Walker, A.K. Chew, H. Li, B. Demir, Z.C. Zhang, G.W. Huber, R.C. Van Lehn, J.A. Dumesic, Universal kinetic solvent effects in acid-catalyzed reactions of biomass-derived oxygenates, *Energy Environ. Sci.* 11 (2018) 617–628, <https://doi.org/10.1039/C7EE03432F>.
- [65] L. Shuai, J. Luterbacher, Organic solvent effects in biomass conversion reactions, *ChemSusChem* 9 (2016) 133–155, <https://doi.org/10.1002/cssc.201501148>.
- [66] T.M.C. Hoang, E. Van Eck, W. Bula, J.G. Gardeneris, L. Lefferts, K. Seshan, Humins based by-products from biomass processing as a potential carbonaceous source for synthesis gas production, *Green Chem.* 17 (2015) 959–972, <https://doi.org/10.1039/C4GC01324G>.
- [67] J. Feng, L. Zhang, J. Jiang, C. Hse, T.F. Shupe, H. Pan, Directional synergistic conversion of lignocellulosic biomass with matching-solvents for added-value chemicals, *Green Chem.* 21 (2019) 4951–4957, <https://doi.org/10.1039/C9GC02365H>.
- [68] M.J. Antal Jr, W.S. Mok, G.N. Richards, Mechanism of formation of 5-(hydroxymethyl)-2-furaldehyde from D-fructose and sucrose, *Carbohydr. Res.* 199 (1990) 91–109, [https://doi.org/10.1016/0008-6215\(90\)84096-D](https://doi.org/10.1016/0008-6215(90)84096-D).